

¹ Modeling ice-shelf cavities and calving tabular
² icebergs

A.A. Stern,¹, A. Adcroft¹ and O. Sergienko¹, G. Marquez¹, R. Hallberg¹

³ **Key Points:**

⁴

A. A. Stern, Geophysical Fluid Dynamics Laboratory, Princeton University

A. Adcroft, Geophysical Fluid Dynamics Laboratory, Princeton University

O. Sergienko, Geophysical Fluid Dynamics Laboratory, Princeton University

G. Marquez, Geophysical Fluid Dynamics Laboratory, Princeton University

R. Hallberg, Geophysical Fluid Dynamics Laboratory, Princeton University

5 **Abstract.** The calving of giant icebergs is an important process in the
6 Antarctic freshwater cycle. Iceberg calving can significantly alter the geom-
7 etry of an ice-shelf cavity, potentially affecting the circulation within the cav-
8 ity. Giant icebergs which break away can drift across large distance, alter-
9 ing regional ocean circulation, sea ice distributions and bottom water for-
10 mation. However, despite its importance, the current generation of numer-
11 ical models is unable to represent this process in a physically realistic way.
12 In this study we develop a model of an ice-shelf cavity using a Lagrangian
13 ice shelf. The ice shelf is constructed out of Lagrangian elements which are
14 bonded together by numerical bonds. This Lagrangian framework allows for
15 large pieces of the ice shelf to break away and become tabular icebergs. The
16 model developed in the manuscript is referred to as the Lagrangian Iceberg/Ice
17 Shelf Model (LIISM). This paper provides a description of the LIISM model
18 and discusses a number of the technical elements involved in building a La-
19 grangian ice shelf. To test the model, the LIISM is used to model an ideal-
20 ized ice-shelf cavity which was developed as part of the Marine Ice Ocean
21 Modeling Inter-comparison Project (MISOMIP). Results from static ice-shelf
22 experiments compare well to results using a more traditional Eulerian ice-
23 shelf models. The novel capabilities of the LIISM are demonstrated by mod-
24 eling a tabular iceberg breaking away from the idealized ice shelf.

1. Introduction

25 Floating ice shelves cover vast regions of the Antarctic polar oceans. These massive
26 platforms of ice extend deep into the water column, applying large pressures to surface
27 of the ocean, which is often hundreds of meters below global sea level. Beneath the ice
28 shelves, both the bottom topography and the ice-shelf geometry play a role in steering
29 ocean currents [Nicholls , 1996; Jenkins et al , 2010; Stern et al , 2014]. The topographic
30 constraint imposed by the ice shelf at the ocean's upper boundary significantly affects the
31 circulation within the ice-shelf cavities, and gives the ocean within the ice shelves cavities
32 a unique character.

33 In addition to suppressing the depth of ocean surface, the ice shelves also melt (and
34 break), thus providing a freshwater flux into the ice-shelf cavities. This melting and
35 breaking of Antarctic ice shelves is a key component in the Antarctic meltwater system.
36 Within the ice-shelf cavities, the input of buoyant meltwater into the ocean creates rising
37 density plumes, which are guided along the ice-shelf base, and help drive ocean circulation
38 beneath the ice shelves [MacAyeal , 1984; Holland and Feltham , 2006]. The strength of
39 the circulation within the cavity feeds back onto the ice-shelf melt rates, by removing cold
40 water from the cavity, and drawing in warmer waters from the open ocean, thus providing
41 the constant supply of thermal energy needed for continuous ice-shelf melt [Lewis and
42 Perkin , 1986; Jacobs et al , 2011].

43 The Antarctic ice shelves are also characterized by large infrequent calving events where
44 massive pieces of the ice shelves break off, to create giant tabular icebergs. Observational
45 estimates suggest that approximately half of Antarctic ice-shelf decay is due to iceberg

46 calving, while the other half occurs through ice-shelf melting [Depoorter et al , 2013;
47 Rignot et al , 2013]. Calving icebergs' sizes appear to fit a power law distribution, with
48 the majority of icebergs being small ($L < 1$ km), while giant tabular icebergs ($L > 5$ km)
49 account for more than 90% of the icebergs mass [Tournadre et al , 2016]. After calving,
50 icebergs slowly drift away from their mother glaciers, often becoming stuck in sea ice, or
51 become grounded along the Antarctic coast [Lichy and Hellmer , 2001; Dowdeswell and
52 Bamber , 2007]. Giant tabular icebergs also extend deep into the water column, and have
53 to potential to disrupt ocean circulation patterns for months or even years after calving
54 [Robinson et al , 2012; Stern et al , 2015].

55 Melt water from both ice-shelf melt and iceberg melt impact the ocean hydrography
56 outside of the ice-shelf cavities, influencing sea ice production and bottom water formation
57 [Arrigo et al , 2002; Robinson et al , 2012; Nicholls et al , 2009]. The long distances traveled
58 by giant icebergs before melting means that their meltwater impact is often felt hundreds
59 of kilometers away from their calving origins [Stern et al , 2016]. Melt water injection (and
60 the accompanying upwelling) from ice shelves and icebergs can also influence biological
61 productivity by providing nutrients to the surface ocean or changing sea ice conditions
62 [Arrigo et al , 2002; Vernet et al , 2012; Biddle et al , 2015]. The increased productivity
63 associated with free-floating tabular icebergs has been linked with local increases in ocean
64 carbon uptake, potentially large enough to be a significant fraction of the Southern Ocean
65 carbon sequestration [Smith et al , 2007].

66 In recent years society's need for improved projections of future sea level has lead to an
67 increased focus on the Antarctic meltwater system described in the previous paragraphs.
68 This increased interest has led to accelerated efforts to accurately model Antarctic ice-shelf

69 cavities [Asay-Davis et al , 2016]. Modeling the ocean beneath the ice shelves presents
70 a unique set of challenges, since (i) the presence of ice shelves provides a rigid upper
71 boundary for the ocean model which is not encountered elsewhere in the ocean, and
72 (ii) melting and breaking ice shelves imply a changing ocean boundary conditions which
73 present numerous numerical difficulties.

74 The earliest models of ocean ice-shelf cavities were developed using a static ice shelves
75 with a fixed shape [Hellmer and Olbers , 1989; Determan and Gerdes , 1994; Grosfeld et
76 al , 1997; Holland and Jenkins , 2001; Losch , 2008]. In these models, ice-shelf melting
77 was represented through salinity and temperature fluxes, while the ice-shelf geometry
78 remained unchanged. Later models of ice-shelf cavities allowed the ice-shelf geometry
79 to evolve as the ice shelf melted, permitting the study of coupled ocean-ice phenomena
80 [Gladish et al , 2012; Sergienko , 2013]. More recently, dynamic ice-shelf models have
81 been coupled the ocean cavity, allowing the study of grounding line migration, which is of
82 key importance for sea level rise projections [Grosfeld and Sandhger , 2004; Goldberg et
83 al , 2012; De Rydt and Gudmundsson , 2016]. As far as we know, all models of ice-shelf
84 cavities to date have neglected ice-shelf breaking and iceberg detachment.

85 In parallel to these efforts to develop ice-shelf cavity models, a number of iceberg drift
86 models have been developed, and have been included in some global General Circulation
87 Models [Bigg et al , 1997; Gladstone et al , 2001; Martin and Adcroft , 2010; Marsh et al ,
88 2015]. These iceberg drift models treat icebergs as Lagrangian point particles, which are
89 advected by the flow, and melt according to certain parameterizations for icebergs melt.
90 Since icebergs are treated as point particles, the iceberg drift models are mostly suitable
91 for modeling smaller icebergs drifting across large distances, and as such iceberg drift

models have mostly been used to represent icebergs smaller than 3.5km on a global scale [Jongma et al , 2009; Martin and Adcroft , 2010; Marsh et al , 2015]. These models are not suitable for modeling larger tabular icebergs, which feel the ocean over many grid cells, depress the ocean surface and change circulation patterns [Stern et al , 2016]. They also not suitable for studying the local effects that icebergs have on the surrounding ocean. For this reason, tabular icebergs ($L > 5\text{km}$) are currently not represented in the iceberg drift models used in climate models, even though observations suggest that tabular icebergs account for the vast majority of the total Southern Hemisphere icebergs mass [Tournadre et al , 2016].

The ice-shelf cavity models and iceberg drift models described above have been developed separately from one another, and have not been designed to be used together in a physically consistent way. As such, it has not been possible to model the calving of tabular icebergs away from an ice shelf, which is an important part of the Antarctic climate system. The goal of this study is to develop a model which combines features of the ice-shelf cavity models and the iceberg drift models, to create an ice-shelf cavity model that is able to calve tabular icebergs. To do this, we create an ice-shelf model out of Lagrangian elements which are ‘bonded’ together by numerical bonds. In this framework, icebergs do not get created when a calving event takes place (as in iceberg drift models), but rather the icebergs ‘break away’ from an existing ice shelf, thus changing the geometry of the ice-shelf cavity. Modeling iceberg calving in a physically consistent way allows us to study the ocean response to iceberg detachment. Also, by allowing icebergs protrude deep into the water column we can study the ocean dynamics around individual tabular icebergs (which was not possible in iceberg drift models).

In all simulation in this study, the shape of the calving iceberg is prescribed. The question of how to correctly prescribe a calving law is undoubtably a very important question, which has rightfully received much attention in recent years [Benn et all , 2007; Alley et al , 2008; Levermann et al , 2012]. Bassis and Jacobs [2013], for example, used a discrete element model (DEM) model to study the generation and propagation of cracks within an ice shelf (not coupled to an ocean model). In this study, we bypass the question of how to correctly calve icebergs or break bonds. Instead we focus on developing a framework to model the ocean response to ice-shelf breaking and the presence of tabular icebergs. This framework of representing ice shelves using a Lagrangian grid might be a step towards including giant tabular icebergs in climate models. Including ice fracture into this model will be a later step.

The model developed in this study is referred to at the Lagrangian Iceberg/Ice Shelf Model (LIISM). Section 2 gives a description of many of the key aspects of the LIISM. Since this model is a new approach to modeling ice-shelf cavities, we present many of the technical elements involved in constructing the model. Those readers who are more interested in the model capabilities, should skip directly to the numerical experiments presented in the later sections. In Section 3 and 4, the LIISM model is used to simulate the circulation beneath an idealized ice shelf. The LIISM model results are validated by comparing them to an existing Eulerian ice-shelf model. We then we move beyond the capabilities of the existing ice-shelf model by allowing a piece of the ice shelf to break away, becoming a tabular icebergs, and consider the ocean response to this calving event.

2. Model description

The LIISM is a Lagrangian particle-based model (or DEM model) in that the objects of the model are Lagrangian elements. Each element represents a mass of ice which is floating in the ocean, and has a position, velocity, mass, and a set of dimensions, which can evolve in time. The motion of each element is determined by a momentum equation which is solved in the (Lagrangian) reference frame of the element. The elements are forced by oceanic and atmospheric forces, which are provided by the user, or are determined by coupling the LIISM to an ocean/atmosphere model. The elements also interact with one another and can be bonded together to form larger structures. In different contexts, the LIISM elements can be thought to represent individual icebergs, sea ice flows, or, when the elements are bonded together, they can represent larger structures such as tabular icebergs or ice shelves.

The LIISM model is developed on the code base of an existing iceberg drift model [Martin and Adcroft , 2010; Stern et al , 2016]. When run with the correct set of runtime flags, the model runs as a traditional iceberg drift model.

2.1. Equations of motion

The elements drift in the ocean, forced by atmosphere, ocean and sea-ice drag forces, as well as the Coriolis force and a force due to the sea surface slope. When these ice elements move alone (without interactions with other elements), they can be thought of as representing of small icebergs, and follow the same equations described in the iceberg drift model of Martin and Adcroft [2010] (based on the equations outlined in Bigg et al [1997]; Gladstone et al [2001]).

156 In addition to the environmental forces, the elements in the LIISM model experience
 157 interactive forces due to the presence of other elements. Two types of interactive forces are
 158 included between elements. The first force is repulsive force which is applied to elements
 159 to prevent them from moving too close to one another. This repulsive force prevents
 160 icebergs from piling up on top of one another. The second interactive force is a force due
 161 to numerical ‘bonds’, and is only applied if two elements are ‘bonded’ together. When
 162 two elements are bonded, each element feels an attractive force that prevents the elements
 163 from moving too far apart from one another. The interactive forces between two bonded
 164 elements are defined such that in the absence of other forces the elements come to rest
 165 adjacent to one another, with no overlap of the iceberg areas.

The momentum equation for each element is given by

$$M \frac{D\vec{u}}{Dt} = \vec{F}_A + \vec{F}_W + \vec{F}_R + \vec{F}_C + \vec{F}_{SS} + \vec{F}_{SI} + \vec{F}_{IA}, \quad (1)$$

166 where $\frac{D}{Dt}$ is the total (Lagrangian) derivative, M is the mass of the element, \vec{u} is the
 167 velocity of the element, and the terms on the right hand side give the forces on the
 168 element due to air drag (\vec{F}_A), water drag (\vec{F}_W), sea ice drag (\vec{F}_{SI}), Coriolis force (\vec{F}_C),
 169 wave radiation force (\vec{F}_R), sea surface slope (\vec{F}_{SS}), and interactions with other elements
 170 (\vec{F}_{IA}). The environmental forces are the same as those presented in Martin and Adcroft
 171 [2010], and are provided for completeness in Appendix A. The details of the interactive
 172 forces are provided in below.

2.2. Interactive Forces

The interactive force on an element is calculated by adding together the interactions with all other elements, such that the interactive force on element i , $(\vec{F}_{IA})_i$ is given by:

$$(F_{IA})_i = \sum_{j \neq i} (F_{IA})_{ij}, \quad (2)$$

where $(F_{IA})_{ij}$ is the force on element i by element j . Both bonded and repulsive interactions are modeled using elastic stresses with frictional damping. The elastic component of the force is a function of the distance between the two elements, while the frictional damping force depends on the relative velocity of the two elements.

To describe the forces between two elements, we begin by introducing some notation. Let \vec{x}_i , \vec{x}_j be the positions of elements i and j . The distance between elements i and j is

$$d_{ij} = |\vec{x}_i - \vec{x}_j|. \quad (3)$$

We then define the interaction diameter of an element by

$$D_i = 2\sqrt{\frac{A_i}{\pi}}, \quad (4)$$

where A_i is the planar surface area of element i . Using this, we define the critical interactive length scale,

$$L_{ij} = \frac{D_i + D_j}{2}, \quad (5)$$

which governs interactions between elements i and j . Repulsive forces are only applied when $d_{i,j} < L_{i,j}$, while bonded forces are only applied when $d_{i,j} > L_{i,j}$ and a bond exists between element i and j . Bond and repulsive forces are designed to such that in the absence of other forces, bonded particles will settle in an equilibrium position where elements are separated by the critical interaction length scale $L_{i,j}$.

To aid in notation, we define a bond matrix B_{ij} such that $B_{ij} = 1$ if elements i and j are bonded together and $B_{ij} = 0$ otherwise. Using this notation, the interactive force $(\vec{F}_{IA})_{ij}$ on an element i by an element j is given by

$$(\vec{F}_{IA})_{ij} = \begin{cases} (\vec{F}_e)_{ij} + (\vec{F}_d)_{ij} & \text{if } d_{ij} \leq L_{ij} \\ (\vec{F}_e)_{ij} + (\vec{F}_d)_{ij} & \text{if } d_{ij} > L_{ij} \text{ and } B_{ij} = 1 \\ 0 & \text{if } d_{ij} > L_{ij} \text{ and } B_{ij} = 0 . \end{cases} \quad (6)$$

$(\vec{F}_e)_{ij}$ and $(\vec{F}_d)_{ij}$ are the elastic and frictional damping components of the interactive force between elements i and j. The elastic force $(\vec{F}_e)_{ij}$ between elements is given by

$$(\vec{F}_e)_{ij} = -\kappa_e \left(d_{i,j} - L_{i,j} \right) T_{i,j} \vec{r}, \quad (7)$$

where $\vec{r} = \frac{(\vec{x}_i - \vec{x}_j)}{|\vec{x}_i - \vec{x}_j|}$ is the directional unit vector between the position of element i and j,

and κ_e is the spring constant, and $T_{i,j}$ is the minimum of the thickness of elements i, j.

We choose $(\vec{F}_b)_{ij}$ proportional to $T_{i,j}$ (the minimum thickness of elements i and j) so the

formulation of interactive forces has the desired property that it obeys Newton's 3rd Law

(i.e.: $(\vec{F}_{IA})_{ij} = -(\vec{F}_{IA})_{ji}$). The minimum thickness is preferred to the average thickness,

since this means that the for two bonded elements a fixed distance apart, acceleration due

to elastic forces is bounded, even when the thickness of one of the elements approaches

zero.

The frictional damping force has components that damp both the relative radial velocity and relative transverse velocities of the two elements. If \vec{r}^\perp is the direction vector perpendicular to \vec{r} , and $P_{\vec{r}}$ and $P_{\vec{r}^\perp}$ are the projection matrices that project onto \vec{r} and \vec{r}^\perp respectively, then the frictional damping force is given by

$$(\vec{F}_d)_{ij} = \left(-c_r P_{\vec{r}} - c_t P_{\vec{r}^\perp} \right) \cdot (\vec{u}_i - \vec{u}_j) \quad (8)$$

Here c_r and c_t are the radial and transverse drag coefficients. For the simulation below,

we set $c_r = 2\sqrt{\kappa_e}$ and $c_t = \frac{1}{4}c_r$ so that the radial elastic force is critically damped, and the

¹⁹² transverse damping is sub critical. The damping forces are implemented using an implicit
¹⁹³ time stepping scheme, to avoid stability issues for very small elements (details found in
¹⁹⁴ Appendix B).

¹⁹⁵ The effectiveness of the repulsive forces can be seen in Figure 1, which shows an uncou-
¹⁹⁶ pled (ice only) simulation where ice elements drift westward into a bay, and eventually
¹⁹⁷ come to rest with minimal overlap between elements. The effectiveness of the numerical
¹⁹⁸ bonds is demonstrated in Figure 2, where tabular icebergs (constructed from many ice
¹⁹⁹ elements bonded together) and individual icebergs (unbonded elements) drift together
²⁰⁰ towards a convex coast line. When the tabular icebergs arrive at the coast, they bump
²⁰¹ into the coastline and begin to rotate, influencing the paths of the other icebergs. In
²⁰² this example we see that modeling large structures using small elements bonded together,
²⁰³ allows us to achieve large-scale structure and rotational motion, without having to include
²⁰⁴ an equation for the angular momentum of the elements (as discussed in Jakobsen [2001]).
²⁰⁵ Animations of these simulations can be found in the supplementary materials.

2.3. Element geometry and packing

²⁰⁶ Elements are packed differently depending on the shape of the elements. For all simula-
²⁰⁷ tions in this study, we use elements whose surface areas are equally-sized regular hexagons.
²⁰⁸ In order to pack these elements together, the hexagonal elements are initially arranged in
²⁰⁹ a staggered lattice, with each element bonded to the adjacent elements (see Figure 3a).
²¹⁰ In this arrangement, each element (away from the edges) is bonded to six other elements.
²¹¹ The bonds between elements form a pattern of equilateral triangles, which give the larger
²¹² structure rigidity.

Some experiments were also performed using rectangular elements, arranged in a regular (non-staggered) lattice. In this case, each element forms four bonds with adjacent elements. However, the resultant structures were found to be much less rigid and tended to collapse when sufficient forces was applied. For this reason, hexagonal elements were preferred.

2.4. Ocean-ice and ice-ocean coupling

The LIISM model is coupled to the ocean model via a two-way synchronous coupling, meaning that ocean model fields are passed to the LIISM model and the LIISM model fields are passed back to the ocean model at every time step. Passing fields between the two models involves interpolating fields between the Eulerian grid of the ocean model and the ‘Lagrangian grid’ of the LIISM model (i.e.: onto the ice elements).

The coupling from the ocean model to the LIISM model is straight forward: at every time step, the ocean mixed layer temperature, salinity, velocity and sea-ice concentration are passed from the ocean model to the LIISM model, to be used in the momentum and thermodynamic equations of the ice elements. Within the LIISM model, the ocean model fields are interpolated onto the Lagrangian grid using a bilinear interpolation scheme. The LIISM model is not sensitive to the chosen interpolation scheme.

The coupling in the other direction, from the LIISM model to the ocean model, is more complex. The LIISM model influences the ocean by: (i) applying a pressure to the ocean surface, (ii) applying a heat, salinity and mass flux to the ocean, associated with ice melting, and (iii) affecting the upper ocean by applying a no-slip boundary condition and frictional velocity beneath the ice. Fields from the LIISM model are interpolated from the Lagrangian grid to the Eulerian ocean grid before they are passed to the ocean

model. Since the LIISM model applies large pressures to the ocean surface, the ocean model is sensitive to the interpolation scheme used to map the LIISM fields to the ocean grid. Sudden jumps to the ocean surface pressure can trigger tsunamis within the ocean model, making the ocean model become unstable.

The interpolation of the LIISM fields onto the ocean grid is done in a way that is consistent with the shape of the elements in the LIISM model (see Section 2.3). Fields are ‘spread’ to the ocean model grid by exactly calculating what fraction of an element’s surface area lies in a particular grid box, and dividing the field in proportion to this fraction. For example, consider a hexagonal element in the LIISM model, which is positioned such that it intersects four ocean grid cells (Figure 3b). In this situation, the mass of the element is divided between these four ocean cells in proportion to the overlap area between the hexagonal element and the grid cell (this fraction is shown by the colors in 3b). An advantage of this approach is that there are no jumps in pressure as an element moves from one grid cell to another.

The numerical calculation of the intersection between hexagons and the ocean grid is simplified by dividing the hexagon into 6 equilateral triangles. This method allows for the intersection to be found even when the hexagon is not aligned with the grid.

The field-spreading scheme is coded with the restriction that an element’s area can only intersect a maximum of four ocean grid cells at a time. A consequence of this is that this sets a limit on the maximum size of elements that can be represented using this model, i.e.: the longest horizontal dimension of an ice element must be smaller than the ocean grid spacing. Larger ice structures are constructed by bonding together smaller elements.

2.5. Thermodynamics

257 The ice elements decay according to a number of melt parameterizations. As the ice
258 elements melt, their mass decreases, and the appropriate salt, mass and heat fluxes are
259 passed to the ocean. In this section we described the melt parametrization for bonded,
260 unbonded and partially bonded elements.

261 As mentioned above, ice elements which do not interact with other elements are modeled
262 identically to the point particle icebergs described in Martin and Adcroft [2010]. These
263 elements melt according to three semi-empirical parametrization for melt commonly used
264 in previous iceberg studies [Gladstone et al , 2001; Martin and Adcroft , 2010]. Three
265 types of iceberg melting are used: basal melt, M_b , melt due to wave erosion, M_e and melt
266 due to buoyant convection, M_v . M_e and M_v are applied to the sides of the ice element,
267 while M_b is applied at the ice element base. The details of M_b . M_v and M_e are given in
268 Appendix A.

269 When multiple elements are bonded together to form larger structures, it is no long
270 appropriate to use the parameterizations for melt developed for individual point-particle
271 icebergs. An element which is completely surrounded by other elements, is meant to
272 represent a piece of ice in the middle of a large structure, and hence will not experience
273 a melt at its sides due to wave erosion or buoyant convection. Also, the iceberg basal
274 melt rate, M_b described above is based on boundary layer theory of flow past a finite
275 plate, and is only appropriate for basal surfaces where the distance from the leading edge
276 is sufficiently small [Eckert , 1950; Weeks and Campbell , 1973]. For an element in the
277 interior of large structures, the distance from the edge of the structure is large, and so
278 using M_b for the basal melt is not appropriate. Instead, the basal melt, M_s is determined

²⁷⁹ using the three equation model for basal melt, which is a typical melting parametrization
²⁸⁰ beneath used beneath ice shelves [Holland and Jenkins , 1999].

When using both individual elements and bonded elements in the same simulation, we determine which melt rate parameterizations to use based on the amount of bonds that each element has. An element which is in the center of a large structure will form the maximum number of bonds, while unbonded elements form zero bonds. If maximum number of bonds that an element can form (given the shape of the element) is N_{max} , and the number bonds that an element has is N_b , then the side melt and bottom melt for that element are given by

$$M_{side} = \frac{(N_{max} - N_b)}{N_{max}}(M_v + M_e) \quad (9)$$

and

$$M_{bottom} = \frac{(N_{max} - N_b)}{N_{max}}M_b + \frac{N_b}{N_{max}}M_s \quad (10)$$

²⁸¹ respectively. In this way, elements with no bonds, melt like point particle icebergs, ele-
²⁸² ments at the center of large structures melt like ice shelves, and elements at the sides of
²⁸³ large structures have a combination of iceberg side and basal melt, and ice-shelf melt.

2.6. Algorithms and computational efficiency

²⁸⁴ Including interactions between elements leads to an increase in the computational com-
²⁸⁵ plexity of the model. In this subsection we comment on some of the algorithmic proce-
²⁸⁶ dures that have been used to increase the computational efficiency. Readers who are not
²⁸⁷ interested in this more technical side of the model should skip this section.

2.6.1. Time stepping

289 The ice elements in the LIISM model are advected using a semi-implicit velocity Verlet
290 time-stepping scheme. The velocity verlet time stepping scheme is commonly used in DEM
291 models in video games because it is computational efficient and has desirable stability
292 properties [Jakobsen , 2001]. This time stepping scheme was preferred to the Runge-
293 Kutta 4, which was used in the iceberg model of Martin and Adcroft [2010] since, the
294 Verlet time stepping only requires one calculation of the interactive forces per time step
295 (while the Runge-Kutta scheme requires the interactive forces to be calculated four times).
296 Since the calculation of the interactive forces is one of the most computationally expensive
297 part of the algorithm, the Verlet scheme leads to a significant increase in the speed of the
298 model. We note that the Verlet scheme used in the LIISM contains a small modification
299 of the original (fully explicit) velocity Verlet time stepping scheme in that damping terms
300 are treated implicitly (which increases the numerical stability). The details of this time
301 stepping scheme are outlined in Appendix B.

302 2.6.2. Interactions and Bonds

303 At every time step, we calculate the force on each element due to interactions with every
304 other element. In principle, this involves order n^2 operations (for n elements). However,
305 since each element only has repulsive interactions with elements that are less than one
306 ocean grid cell away, and each element only has bonded interactions with a small number
307 of other elements, we are able to reduce the complexity of the system.

308 The complexity reduction is achieved by storing the element data in an efficient way
309 that prevents having to search through all element pairs to check if they are close to
310 one another or are bonded with one another. The data storage system works as follows:
311 pointers to the memory structures containing each element are stored in linked list data

312 structures, which allow elements to be added and removed from the lists easily without
313 restructuring the entire list. Instead of using one list for all the elements on a processor,
314 we use a separate linked list for each ocean grid cell. When an element moves between
315 ocean grid cells, it is removed from its original list and added to the list corresponding to
316 its new ocean grid cell. Since the area of elements has to be smaller than the area of an
317 ocean grid cell, the critical interaction length scale (equation 5) is less than the length of
318 a grid cell. This means that elements only experience repulsive forces with elements in
319 the same ocean grid cell, or in one of the 8 adjacent cells. Limiting the possible repulsive
320 interactions to elements in these 9 linked lists substantially reduces the computational
321 time needed to calculate the total interactive force.

322 Bonded interactions are handled slightly differently. Each bond is assigned a piece of
323 memory. Each ice element contains a linked list of each of its bonds (typically up to six
324 bonds per element). At each time step, the code traverses the lists of bonded elements,
325 and adds a bonded force corresponding to these bond. The bonded force is only applied
326 if $\vec{r}_{i,j} > L_{ij}$, to avoid double counting an interaction. Having a list of bonds stored with
327 each element reduces the computational complexity of bonded interactions from order n^2
328 to order n. Handling bonded attractive forces separately to the repulsive and non-bonded
329 forces means that we do not need to check whether two elements are bonded, which further
330 increases the computational efficiency.

331 **2.6.3. Parallelization and halos**

332 The LIISM model runs on multiple processors in parallel. When elements move from
333 an ocean cell on one processor to an ocean cell on a second processor, the memory has to
334 be passed from one processor the next, added and removed to the appropriate lists and

335 the memory has to be allocated and deallocated correctly. Element interactions across
336 the edge of processors are handled using computational halos. A computational halo is a
337 copy of the edge of a one processor which is appended to the edge of a second processor,
338 so that the first processor can ‘see’ the second processor during a time step. Before a
339 time step, elements at the edges of each processor are copied onto the halos of adjacent
340 processors so that they can be used in calculating the interactive forces. After each time
341 step, these halos are removed, and the process is repeated. These halo updates are one
342 of the most computationally expensive parts of the LIISM model.

343 Keeping track of pairs of bonded elements that move across a processor edge requires
344 a lot of book keeping since bonds have to be severed and reconnected. Details of how
345 the bonds are broken and reconnected across processor boundaries are provided in Ap-
346 pendix C.

3. Experiment Setup

347 The introduction of Lagrangian elements, numerical bonds and interpolation schemes
348 between the Eulerian and Lagrangian grids (discussed in Section 2) means that we are
349 now able to model ice-shelf cavities which undergo large calving events. We demonstrate
350 this capability by performing numerical experiments with the LIISM model coupled to
351 the MOM6 ocean model [Hallberg et al , 2013].

3.1. MISOMIP configuration

352 In order for our (pre-calving) simulations to be easily comparable to previous models
353 of ice-shelf cavities, we use an experimental setup based on the configuration created
354 for the Marine Ice Ocean Modeling Inter-comparison Project (MISOMIP) [Asay-Davis et

³⁵⁵ al , 2016]. The MISOMIP configuration was developed as a standardized configuration
³⁵⁶ to allow for a comparison between various ocean-ice coupled models. The configuration
³⁵⁷ consists of an idealized ice shelf in a rectangular domain. The domain is $L_x = 80\text{km}$ wide
³⁵⁸ and $L_y = 480\text{km}$ long, and contains an ice shelf which is grounded on the south side of
³⁵⁹ the domain and has an ice front at $y=650\text{km}$. The ice thickness and bottom topography
³⁶⁰ of this setup are shown in Figure 4a and 4b respectively, with the grounding line position
³⁶¹ drawn in for reference. The configuration is the same as that of the Ocean0 setup in the
³⁶² MISOMIP, with three changes made:

- ³⁶³ 1. The ‘calving criteria’ used in the MISOMIP study (which states that all points in
³⁶⁴ the ice shelf with thickness less than 100m are set to zero thickness) has not been used.
- ³⁶⁵ 2. The ice shelf has been thickened on the flanks of the domain, so that the latitude of
³⁶⁶ the grounding line increases away from the center of the ice shelf.
- ³⁶⁷ 3. The ice shelf is configured to be symmetric about its meridional center line ($x = \frac{L_x}{2}$).

³⁶⁸ This was achieved by using the average of the left and right flanks of the ice-shelf thickness.
³⁶⁹ These three changes were made in order to make the circulation beneath the ice shelf
³⁷⁰ easier to interpret.

³⁷¹ The LIISM model is coupled to the MOM6 ocean model. The ocean model is run in
³⁷² using vertical coordinate system which is a hybrid between a sigma-level and a z-level
³⁷³ coordinate. In particular, model layers bend underneath the ice shelf as they would in a
³⁷⁴ sigma model, but collapse to zero thickness when they intersect with bottom topography,
³⁷⁵ as they would in a z-level model. The coordinate system was achieve using ALE regridding-
³⁷⁶ remapping scheme [White et al , 2009]. The model used a horizontal resolution of 2km,
³⁷⁷ and 72 vertical layers. All simulation were repeated using the ocean model is run layered

mode (results were similar and are not presented here). Ocean parameters are as specified in the MISOMIP configuration [Asay-Davis et al , 2016], and are shown in Table 1. The simulation is initially at rest, with horizontally uniform initial ocean temperature (Figure 5a) and salinity profiles that vary linearly between specified surface and bottom values. The initial surface temperature and salinity are $T_t = -1.9^{\circ}\text{C}$ and $S_t = 33.8 \text{ psu}$, respectively. The initial temperature and salinity at the depth H_{ocean} are $T_b = 1.0^{\circ}\text{C}$ and $S_b = 34.7 \text{ psu}$. The maximum ocean depth is $H_{ocean} = 720 \text{ m}$. A sponge layer is used on the northern boundary, which relaxes back to the initial temperature and salinity with a relaxation time scale of $T_{sponge} = 0.1 \text{ days}$. Melting is set to zero for ocean cells where the ocean column thickness is less than 10m to avoid using more energy to melt ice than is present in the water column.

3.2. Initializing Lagrangian elements:

Ice elements in the LIISM model are set to be hexagonal and are arranged in a regular staggered lattice (as discussed in Section 2.3). The sides of the gridded hexagons are initialized with length $S = 0.98 \text{ km}$. Recall that the element size must be smaller than the ocean grid spacing (i.e.: $2S < \Delta x = 2 \text{ km}$). Gaps along the boundaries are filled in using smaller elements so that the total ice-shelf area is preserved. The initial mass of the ice elements is determined by a preprocessing inversion step, which is the inverse of the 'mass-spreading' interpolation procedure discussed in Section 2.3.

Figure 4c shows what the ice-shelf draft would be if the draft were calculated from the mass of elements in each ocean grid cell without spreading an element's mass across neighboring cells (i.e.: treating elements as point masses). Figure 4b shows the draft after spreading the mass across grid cells. When the mass spreading interpolation scheme is

400 not used, grid artifacts seen in the ice-shelf draft (Figure 4c). The grid artifacts are much
401 reduced when the mass spreading interpolation is used (Figure 4b).

3.3. Numerical experiment

402 1. Static ice-shelf experiment:

403 In the first experiment, we use a static ice shelf where the velocity of all ice elements is set
404 to zero. In this experiment, the ice shelf is thermodynamically active and is able to ‘melt’
405 but has a constant thickness (as in the Ocean0 experiment in the MISOMIP [Asay-Davis
406 et al , 2016]). In this setup, ice-shelf melting generates a temperature and salinity flux
407 into the ocean, but does not change the thickness of the ice shelf. This can be thought to
408 represent an ice shelf in dynamic equilibrium where the melt is exactly balanced ice-shelf
409 advection.

410 Results of the static ice-shelf experiment using the LISSM model are compared to the
411 results from an existing Eulerian ice-shelf cavity model [Goldberg et al , 2012], run in
412 an identical configuration (using the ice draft from Figure 4b). Results from the static
413 ice-shelf experiment are analyzed after 5 years of model spinup.

414 2. Tabular iceberg calving:

415 Next, we preform a numerical experiment which demonstrates capabilities of the LIISM
416 model that can not be performed by traditional Eularian ice-shelf models. In this exper-
417 iments we break off a large piece of the ice shelf and allow it to drift into the ocean as a
418 tabular iceberg.

419 All ice elements initially within a 14.4 km radius of the center of the ice front are allowed to
420 move freely while the other ice elements continue to be held are stationary. Ice elements
421 less than 12 km from the center of the ice front, are bonded together to form a semi-

422 circular tabular iceberg. A ring of elements whose distance, d , from the ice front center
423 obeys $12 \text{ km} \leq d \leq 14.4 \text{ km}$, are allowed to move freely, but have all their bonds removed.
424 Elements in this half annulus represent fragments of the ice shelf which calve into small
425 pieces during a large calving event. Breaking the bonds of these surrounding elements
426 allows the tabular iceberg to move away from the ice-shelf cavity more easily.

427 A wind stress $\vec{\tau} = <0.05, 0.05> \frac{N}{m^2}$ is applied to drive the tabular iceberg away from the
428 ice-shelf cavity. Perturbation experiments were performed using other wind stress values.
429 The tabular iceberg calving experiment is initialized using the ocean state from the static
430 ice-shelf experiment after 5 years of simulation time. In tabular iceberg calving experi-
431 ment, the ice shelf and icebergs are allowed to decay as they melt.

4. Results

4.1. Static ice-shelf experiment

432 The LIISM results from the static ice-shelf experiment fit well within the current under-
433 standing of ice-shelf cavity circulations based on ice-shelf observations [MacAyeal , 1984;
434 Lewis and Perkin , 1986; Jacobs et al , 2011] and previous modeling efforts [Determan and
435 Gerdes , 1994; Holland and Feltham , 2006; Losch , 2008]. The initial water temperatures
436 inside the domain are warmer than the in-situ freezing point, and cause melting at the
437 ice-shelf base. The melt water entering the domain is more buoyant than the water around
438 it, and rises along the ice shelf as a cool fresh plume (Figure 5b, c). As the plume rises, it
439 entrains ambient water causing a warming of the upper ocean (Figure 5b). This injection
440 of positive buoyancy at depth drives a clockwise circulation outside of the ice-shelf cavity
441 (Figure 7a), providing the ice-shelf cavity with a continuous supply of warm water which
442 provides the thermal energy required for continuous ice-shelf melt.

443 The highest melt rates are observed within 100km of the grounding line (Figure 6a).
444 These elevated melt rates are caused by the presence of warm water (Figure 6d) and
445 increased ocean velocities (Figure 6c) near the grounding line, as well as the fact that
446 freezing point of ice decreases with increasing pressure. Elevated melt rates are also seen
447 near the ice front, caused by strong currents running along the ice-shelf front.

448

449 Comparison of LIISM and Eulerian ice-shelf model

450 The LIISM results from the static ice-shelf experiment are qualitatively similar to most
451 of the simulations from the MISOMIP experiment [Asay-Davis et al , 2016], which use a
452 similar configuration. To get a quantitative comparison, we compare the LIISM results
453 to a simulation using an Eulerian ice-shelf model with an identical configuration. The
454 results show that two simulations have very similar circulations (Figures 7), melt rates
455 and temperature/salinity profiles (see supplementary materials). The differences between
456 the barotropic stream functions of the two simulations (for example) are two orders of
457 magnitude smaller than the differences between two simulations using the same Eulerian
458 ice shelf with different vertical coordinate systems [double check that this is correct].

459 The good agreement between the Eulerian and Lagrangian simulations is not too sur-
460 prising since the two models are coupled to the same ocean model in exactly the same
461 configuration. Recall that the role of the ice-shelf model in these simulations is to (i)
462 apply a pressure to the ocean surface, (ii) provide melt fluxes based on the three equa-
463 tion model, and (iii) alter the upper ocean boundary condition below the ice shelf. The
464 agreement between the Eulerian and Lagrangian simulations is a confirmation that these
465 three tasks are being done correctly within the LIISM model, and that the LIISM is able

⁴⁶⁶ to model sub-ice-shelf cavities as well as the Eulerian model does. This is a good starting
⁴⁶⁷ point for moving beyond the capabilities of the Eulerian model.

4.2. Tabular iceberg calving experiment

⁴⁶⁸ The tabular iceberg calving experiment demonstrates that the model is able to simulate
⁴⁶⁹ a tabular iceberg being calved from an ice shelf (see animations of in the supplementary
⁴⁷⁰ materials). After the numerical bonds are severed, the tabular iceberg and smaller ice
⁴⁷¹ fragments calve away from the ice shelf and begin to move. The tabular iceberg drifts
⁴⁷² to the northward east, driven by the wind and steered by the Coriolis force (Figure 8,
⁴⁷³ 9). After the iceberg has moved away from the ice shelf, we observed a warming of the
⁴⁷⁴ surface waters nearby ice front and iceberg edge (Figure 10). This surface warming is
⁴⁷⁵ caused by an upwelling of the warmer waters from beneath the ice shelf and iceberg. As
⁴⁷⁶ the icebergs drifts away from the ice front, these warmer waters remain at the surface,
⁴⁷⁷ mapping of the wake of the iceberg (Figure 10). The signature of upwelling water in the
⁴⁷⁸ wake of a drifting tabular iceberg bears some similarity to satellite observations of streaks
⁴⁷⁹ of increased ocean color in the wake of tabular iceberg in the Southern Ocean [Duprat et
⁴⁸⁰ al , 2016], suggesting that the increased productivity around iceberg may be driven by
⁴⁸¹ upwelling water delivering nutrients to the surface.

⁴⁸² The motion of the tabular iceberg disturbs the ocean surface, which drives ocean ve-
⁴⁸³ locities through out the water column (Figure 11). The elevated velocities around the
⁴⁸⁴ tabular iceberg lead to increased vertical mixing in the vicinity of the iceberg, which
⁴⁸⁵ alters the stratification of the water column (Figure 9), heating the upper ocean. The
⁴⁸⁶ increased ocean velocities and increased surface temperatures cause elevated melt rates
⁴⁸⁷ at the base of the ice shelf and iceberg (Figure 12). Large melt rates are observed at the

488 newly calved ice-shelf front and on the rounded side of the iceberg (Figure 12a), where
489 the iceberg calving has created steep ice cliffs. These sharp ice fronts allow for large ocean
490 currents (Figure 12c), which drive the elevated melt rates. These elevated melt rates act
491 to smooth out the ice front over time, making the ice cliff less steep. While this is likely
492 a real phenomena that could be observed in nature, we should be wary of the modeled
493 velocities at the ice cliffs, since large changes in ice-shelf thicknesses are often associated
494 with numerical pressure gradient errors which can drive spurious motion.

495 As mentioned above, the direction (and speed) of the iceberg drift is largely determined
496 by the wind speed and direction. Perturbation experiments using different wind stresses
497 showed that for sufficiently large winds, the iceberg drifts to the north east when the
498 zonal component of the wind stresses is positive, and to the north west when the zonal
499 component of the wind stress is negative. For a purely zonal wind stress with $\tau_x \leq 0.01 \frac{N}{m^2}$,
500 the iceberg does not move away from the ice shelf. When the wind is purely offshore
501 ($\tau_x = 0.0 \frac{N}{m^2}$), a meridional wind stress $\tau_y \geq 0.05 \frac{N}{m^2}$ is needed to move the tabular iceberg
502 away from the ice shelf. While this result is partly an artifact of the artificial shape of the
503 calving iceberg, it is also consistent with Bassis and Jacobs [2013] who noted that calving
504 is a two step process consisting of (i) ice-shelf breaking and (ii) iceberg detachment. The
505 results here suggest that strong (cross-shore) winds may be required to drive large tabular
506 icebergs away from their mother glaciers.

507 Finally, we note that the numerical bonds in the LIISM model are needed in order to
508 allow the tabular iceberg to retain its shape. Comparing the iceberg calving simulation
509 with an identical simulation where all numerical bonds have been removed, shows that
510 in the absence of the bonds, the ice elements quickly disperse (Figure 13). In this case,

511 the model behavior is more similar to an ice-shelf disintegration and does not create a
512 cohesive tabular iceberg.

5. Discussion

513 In order to accurately project future sea level, it is likely that we will need to develop
514 fully-coupled global general climate models (GCM's) with dynamic ice-shelf cavities which
515 are able to melt, break and interact with the ocean in physically realistic ways. In the
516 sections above, we have seen that constructing ice shelves out of Lagrangian elements is a
517 potentially useful method for introducing breakable ice shelves and tabular icebergs into
518 climate models. In this section we briefly discuss a few of the things which still need to
519 be done in order to introduce this technology into next generation GCM's.

520 One element which is missing from the LIISM ice shelf is that the ice shelf is not
521 dynamic. Real-world ice shelves are non-Newtonian fluids which are able to flow, allowing
522 the ice-shelf geometry to change over time. Much progress has been made in modeling ice-
523 shelf flows in an Eulerian framework [Grosfeld and Sandhger , 2004; Goldberg et al , 2012;
524 De Rydt and Gudmundsson , 2016]. A challenge will be to develop models with similar
525 ice dynamics in a Lagrangian framework. This can perhaps be achieved using smooth
526 particle hydrodynamics (SPH) methods, which allow partial differential equations to be
527 solved on a Lagrangian grid [Liu and Liu , 2010; Pan et al , 2013]. However, it is presently
528 unclear how one would evolve the numerical bonds over time, so the bonds could still be
529 used to hold the ice shelf and tabular icebergs together. This may involve performing
530 a regridding of the ice element or a regridding of the numerical bonds after severa time
531 steps, or perhaps allowing the numerical bonds to break and form in a dynamic way.

532 The other major innovation which will need to be introduced is a method for breaking
533 numerical bonds. This is essentially equivalent to determining an ice-shelf calving law,
534 and is a famously difficult problem. One possible way that this could be done is to break
535 bonds when the elastic stress in the bond is larger than a given yield stress of that bond.
536 The yield stress in the bond would likely be proportional to the ice thickness. The bond
537 strength could also evolve dynamically as bonds get ‘damaged’. The evolution of bond
538 damage could be tracked using damage mechanics, as has been done in some Eulerian
539 ice-shelf studies [Pralong and Funk , 2005; Borstad et al , 2012].

540 In addition to these two problems, more work needs to be done to determine the in-
541 teraction between tabular icebergs and sea ice, as the presence of sea ice can arrest the
542 motion of tabular icebergs and the presence of icebergs likely affects sea ice formation
543 and dynamics. A possible path towards this is to model sea ice using a Lagrangian grid
544 [Hopkins , 1996; Li et al , 2014], and to treat sea ice - iceberg interactions in the same
545 way that iceberg - iceberg interactions are treated in this study. A number of preliminary
546 experiments have been run using the LIISM model with some ice element representing
547 collections of sea ice flows, and have yielded interesting results (to be presented elsewhere).

548 Finally, there are a number of other open questions associated with introducing giant
549 tabular icebergs into climate models: (i) how to correctly link tabular icebergs’ melt
550 water fluxes to ocean biology, (ii) how to deal with giant calving events in small ensemble
551 simulations where one calving event can skew the ensemble statistics, (iii) how to introduce
552 tabular icebergs into models which do not use a fully dynamic ice sheet, and (iv) how
553 to model the breakup and fracture of freely-floating tabular icebergs. These and other
554 questions will need to be answered in order to achieve physically realistic tabular icebergs

and ice shelves in GCM's. The results presented in this study suggest that coupling DEM models to dynamic ocean models, presents a promising path towards a more realistic representation of breakable ice shelves and icebergs in climate models.

6. Appendix A

6.1. Environmental forces on ice elements

The non-interactive forces on an ice element are as described in [Martin and Adcroft , 2010], and are repeated here for completeness. The forces on an element due to air (a), ocean (o) and sea ice (si) drag are given by

$$(\vec{F}_a) = \rho_a(0.5c_{a,v}WF + c_{a,h}LW)|\vec{u}_a - \vec{u}|(\vec{u}_a - \vec{u}), \quad (11)$$

$$(\vec{F}_o) = \rho_o(0.5c_{o,v}W(D - T_{si})F + c_{o,h}LW)|\vec{u}_o - \vec{u}|(\vec{u}_o - \vec{u}), \quad (12)$$

$$(\vec{F}_{si}) = \rho_{si}(0.5c_{si,v}WT_{si}F + c_{si,h}LW)|\vec{u}_{si} - \vec{u}|(\vec{u}_{si} - \vec{u}). \quad (13)$$

Here ρ_a , ρ_o , ρ_{si} , are the density of air, ocean and sea ice, respectively. $c_{a,v}$, $c_{o,v}$ and $c_{si,v}$ are the vertical drag coefficients with air, ocean and sea ice, while $c_{a,h}$, $c_{o,h}$ and $c_{si,h}$ are the respective horizontal drag coefficients. \vec{u}_a , \vec{u}_o , \vec{u}_{si} , are the velocities air, ocean and sea ice, respectively. L, W, T, F and D are the length, width, thickness, freeboard and draft of the ice element. The element thickness is related to the draft and freeboard by $T = F + D$ and $D = \frac{\rho}{\rho_o}T$, where ρ is the ice element density.

The wave radiation force (\vec{F}_R) is given by

$$\vec{F}_R = \frac{1}{2}\rho_o c_r g a \min(a, F) 2 \frac{WL}{W + L} \frac{\vec{v}_a}{|\vec{v}_a|} \quad (14)$$

where g is the acceleration due to gravity, a is the wave amplitude empirically related to the wind speed by $a = 0.010125|\vec{v}_a - \vec{v}_o|$, and c_{wd} is the wave drag coefficient defined as

$$c_{wd} = 0.06 \min \left(\max \left[0, \frac{L - L_c}{L_t - L_c} \right], 1 \right), \quad (15)$$

where $L_w = 0.32|\vec{v}_a - \vec{v}_o|^2$ is an empirical wave length, $L_c = 0.125L_w$ is the cutoff length, and $L_t = 0.25L_w$ is the upper limit.

The pressure gradient force is approximated as a force due to sea surface slope and given by

$$\vec{F}_{SS} = -Mg\vec{\nabla}\eta \quad (16)$$

where η is the sea surface height.

6.2. Melt rate parametrization

As discussed in Section 2.5, unbounded ice elements in the LIISM model decay according to parameterizations for iceberg decay typically used in iceberg drift models [Martin and Adcroft , 2010], while ice elements within larger ice structures have only a basal melt given by the three equation model [Holland and Jenkins , 1999] .

For unbonded ice elements, the element thickness decays due to basal melt at a rate M_b , while the length and width of the elements decay as a result of melt due to wave erosion, M_e , and melt due to buoyant convection, M_v . Following Martin and Adcroft [2010], the basal melt rate, wave erosion melt rate, and buoyant convection melt rate are parameterized by

$$M_b = 0.58|\vec{v} - \vec{v}_0|^{0.8} \frac{\tilde{T}_0 - \tilde{T}}{L^{0.2}} \quad (17)$$

$$M_e = \frac{1}{12}S_s \left(1 + \cos [\pi A_i^3] \right) \left(\tilde{T}_0 + 2 \right), \quad (18)$$

$$M_v = \left(7.62 \times 10^{-3} \right) \tilde{T}_0 + \left(1.29 \times 10^{-3} \right) \tilde{T}_0^2. \quad (19)$$

\tilde{T} is the effective iceberg temperature and is set to $\tilde{T} = 4^\circ\text{C}$, \tilde{T}_0 is the temperature at the top of the ocean, A_i is the sea ice area fraction, and S_s is the sea state, which is given by the Beaufort scale

$$S_s = \frac{2}{3} |\vec{u}_a - \vec{u}_o|^{\frac{1}{2}} + \frac{1}{10} |\vec{u}_a - \vec{u}_o| \quad (20)$$

571 All three melt rates are in units of meters per day.

572 For elements inside larger structures, the melt due to wave erosion and melt due to
 573 buoyant convection are set to zero, and the basal melt, M_s is given by the standard three
 574 equation model [Holland and Jenkins , 1999].

7. Appendix B

7.1. Modified Verlet Algorithm

575 The LIISM model uses a version velocity verlet time-stepping algorithm, which has been
 576 modified to allow part of the forcing to be calculated implicitly. The traditional velocity
 577 verlet algorithm is commonly used in molecular dynamics, as it is simple to implement,
 578 second order accurate and computationally efficient [Swope et al , 1982; Omelyan et al ,
 579 2002]. Here we modify the tradition scheme to allow for the drag forces to be modeled
 580 implicitly, which prevents large accelerations for element's whose mass approaches zero.

581 To do this, we modify the traditional verlet algorithm to include both an implicit and
 582 explicit acceleration, $a(t) = a_{exp}(t) + a_{imp}(t)$. The explicit acceleration, $a_{exp}(t)$ includes all
 583 forcing terms which depend only on the previous time step, while the implicit acceleration,
 584 $a_{imp}(t)$ includes forcing terms which depend on the current time step (in particular the
 585 drag and Coriolis forces).

586 Using a time step of Δt and the notation $t_{n+1} = t_n + (\Delta t)$, the modified velocity verlet
 587 scheme can be written as:

$$588 \quad 1) \quad x(t_{n+1}) = x(t_n) + u(t_n)\Delta t + \frac{1}{2}\Delta t^2 \left(a_{exp}(t_n) + a_{imp}(t_n) \right).$$

589 2) Calculate $a_{exp}(t_{n+1})$ and $a_{imp}(t_{n+1})$

$$590 \quad 3) \quad u(t_{n+1}) = u(t_n) + \frac{\Delta t}{2} \left(a_{exp}(t_n) + a_{exp}(t_{n+1}) \right) + (\Delta t)a_{imp}(t_{n+1})$$

591 This scheme reduces to the traditional velocity verlet when a_{imp} is set to zero. Note that at
 592 step 2, $a_{exp}(t_{n+1})$ is an explicit function of $x(t_{n+1})$ and other quantities evaluated at time
 593 t_n , while $a_{imp}(t_{n+1})$ additionally depends on $u(t_{n+1})$, and needs to be solved implicitly).

594 For this reason, steps 2 and 3 need to be solved simultaneously, as described in the next
 595 subsection.

596 In equation (1), the forces due to ocean drag, atmospheric drag and sea ice drag are
 597 treated implicitly. The force due to sea surface slope and wave radiation are treated
 598 explicitly. The Coriolis term is handled using Crank-Nicolson scheme so that half of the
 599 effect is implicit and half is explicit. The elastic part of the interactive forces is treated
 600 explicitly, while the interactive damping is handled semi-implicitly in that the drag force
 601 on element A by element B depends on the velocities of elements A and B evaluated at
 602 time t_{n+1} and t_n , respectively.

7.2. Solving for the velocity implicitly

Since this modified scheme contains some forcing terms which are handled implicitly, steps 2 and 3 need to be solved together. We demonstrate how this is done, using a simplified one-dimensional version of equation (1), neglecting the atmospheric drag, sea ice drag and Coriolis force, so that the only implicitly treated term is the ocean drag. We also define an explicit force F_{exp} , which accounts for all forces not proportional the

element velocity. With these simplifications, the implicit and explicit accelerations are

$$a_{exp} = \frac{1}{M}(\vec{F}_{exp}) \quad (21)$$

$$a_{imp} = \frac{1}{M}(F_o) \quad (22)$$

The ocean drag force at time t_{n+1} is modeled (mostly) implicitly as

$$F_W(t_{n+1}) = \tilde{c}_o|u_o(t_n) - u(t_n)|(u_o(t_n) - u(t_{n+1})), \quad (23)$$

where \tilde{c}_o is the effective drag coefficient, accounting for the dimensions of the ice element
 (see equation 12).

Step 3 of the modified velocity verlet scheme can be rewritten by introducing an intermediate velocity u^* , which only depends on the velocity and acceleration at time t_n ,

$$u^*(t_n) = u(t_n) + \frac{1}{2}(\Delta t)a(t_n). \quad (24)$$

Using this, the updated velocity (Step 3) can be written

$$u(t_{n+1}) = u^*(t_n) + \frac{\Delta t}{2}a_{exp}(t_{n+1}) + (\Delta t)a_{imp}(t_{n+1}). \quad (25)$$

Including the forcing terms into this equations gives

$$u(t_{n+1}) = u^*(t_n) + \frac{\Delta t}{2M}(F_{exp}(t_{n+1})) + \frac{\Delta t}{M}\left(c_w|u_o(t_n) - u(t_n)|(u_o(t_n) - u(t_{n+1}))\right) \quad (26)$$

Solving for $u(t_{n+1})$ in terms of quantities which only depend on the previous time step gives

$$u(t_{n+1}) = \frac{u^*(t_n) + \frac{\Delta t}{2M}(F_{exp}(t_{n+1})) + \frac{\Delta t}{M}\left(c_w|u_o(t_n) - u(t_n)|(u_o(t_n))\right)}{\left(1 + \frac{\Delta t}{M}c_w|u_o(t_n) - u(t_n)|\right)} \quad (27)$$

Once the $u(t_{n+1})$ has been found, it can be used to calculated the explicit and implicit accelerations, which are required for the next time step.

607 Finally, we note that the the drag term (equation 23) is not entirely implicit, since the
 608 element velocity inside the absolute value is evaluated at time t_n , rather than at time t_{n+1} .
 609 This is done so that we can solve for the updated velocity analytically. One consequence
 610 of this is that it gives rise to a small oscillation in the element velocity. This oscillation is
 611 addressed by using a predictive corrective scheme: once you have solved for a first guess
 612 of the velocity at time t_{n+1} , this estimate of the velocity is used to update the estimate
 613 of the drag force (i.e.: inside the absolute value signs). Using the updated drag, you can
 614 now repeat the process described above to find an improved estimate of the velocity. We
 615 found that two iterations were sufficient to remove the unwanted oscillation.

616 The procedure described in this section is easily extended to include more forcing terms
 617 and two dimensions (where it involves inverting a 2×2 matrix).

8. Appendix C

618 Connecting bonds across processor boundaries

619 Since the LIISM model can be parallelized across multiple processors, it often happens
 620 that two elements on different processes are bonded together. Keeping track of numerical
 621 bonds across processor boundaries requires a lot of book keeping. In this section we
 622 describe the how LIISM model avoids segmentation faults by severing and reconnecting
 623 bonds at the edge of a processor during halo updates.

624 The basics of the bond bookkeeping work as follows: consider an element A and an
 625 element B that are bonded together. Each element has a copy of the bond (a piece
 626 of memory which describes the bond between the two elements), which is stored with
 627 the element. Let A-B be the bond stored by element A, and B-A be the bond stored

628 by element B. Bond A-B contains a pointer which points to element B and bond B-A
629 contains a pointer which points to element A.

630 Consider a situation where element A and B are originally on Processor 1, and then
631 element B moves to Processor 2. When this occurs, the memory assigned to element B
632 on processor 1 is removed, and is allocated on Processor 2. This means that the pointer
633 to element B in bond A-B (stored in element A on Processor 1) is no longer assigned.

634 Similarly, the pointer to element A in bond B-A (stored in element B on Processor 2) is
635 no longer assigned. Before the next time step, a halo update occurs, so that there is
636 a copy of element A in the halo of Processor 2 and a copy of element B in the halo of
637 Processor 1. After the halo update, the bonds A-B and B-A have to be reconnected on
638 both Processor 1 and 2. To aid in reconnecting the bonds, a copy of the grid cell number
639 of element B is stored in the bond A-B and a copy of the grid cell number of element A
640 is stored in the bond B-A. We refer to this as the ‘most recent address’. Before a bond
641 is moved from one processor to another, the ‘most recent address’ is updated, so that the
642 bond can be reconnected later. To reconnect bond A-B on Processor 1 (for example), we
643 find the most recent address of element B, and search through the list of elements in the
644 grid cell corresponding to the most recent address of element B until element B is found.

645 The pointer to element B in bond A-B is reassigned and the bond is said to be connected.

646 Once all bonds are reconnected, a bond quality control is done where we loop through
647 all bonds and check that they are working properly. To check that a bond is working
648 properly is a four step process. For example, consider the bond A-B stored in element A
649 on Processor 1. To check the quality of this bond, we use the following four steps:

- 650 1. Check that the pointer to element B is assigned on bond A-B (stored on element
651 A).

652 2. Check that the corresponding bond B-A exists on element B.

653 3. Check that a pointer to element A exists in this bond B-A.

654 4. Check that the element A which is being pointed to is the same element A where
655 you started.

656 All four of these tests must pass in order to make sure that the memory is correctly
657 assigned. A useful tool in this process is that each element is assigned a unique number
658 so that elements are easily identified.

9. Possibly add

9.1. Orientation

659 Possibly add a section where we spread mass using the orientation of the icebergs.

References

- 660 Asay-Davis, X. S., S. L. Cornford, B. K. Galton-Fenzi, R. M. Gladstone, G. H. Gudmundsson, D. M. Holland, P. R. Holland, and D. F. Martin (2016), Experimental design for
661 three interrelated marine ice sheet and ocean model intercomparison projects: MIS-
662 MIP v. 3 (MISMIP+), ISOMIP v. 2 (ISOMIP+) and MISOMIP v. 1 (MISOMIP1).
663 *Geoscientific Model Development* 9, no. 7: 2471.
- 664 Arrigo, K. R., G. L. van Dijken, D. G. Ainley, M. A. Fahnestock, and T. Markus (2002).
665 Ecological impact of a large Antarctic iceberg. *Geophys. Res. Lett.*, 29(7).
- 666 Alley, R. B., H. J. Horgan, I. Joughin, K. M. Cuffey, T. K. Dupont, B. R. Parizek, S.
667 Anandakrishnan, and J. Bassis (2008), A simple law for ice-shelf calving. *Science* 322,
668 no. 5906, 1344-1344.
- 669 Bassis, J. N., and S. Jacobs (2013), Diverse calving patterns linked to glacier geometry.
670 *Nature Geoscience*, 6(10), 833-836.
- 671 Benn, D. I., C. R. Warren, and R. H. Mottram (2007). Calving processes and the dynamics
672 of calving glaciers. *Earth-Science Reviews*, 82(3), 143-179.
- 673 Bigg, G. R., Wadley, M. R., Stevens, D. P., and Johnson, J. A. (1997), Modeling the
674 dynamics and thermodynamics of icebergs. *Cold Regions Science and Technology*, 26(2),
675 113-135.
- 676 Borstad, C. P., A. Khazendar, E. Larour, M. Morlighem, E. Rignot, M. P. Schodlok, and
677 H. Seroussi (2012), A damage mechanics assessment of the Larsen B ice shelf prior to
678 collapse: Toward a physically-based calving law, *Geophys. Res. Lett.*, 39, L18502
- 679 Biddle, L. C., J. Kaiser, K. J. Heywood, A. F. Thompson and A. Jenkins (2015), Ocean
680 glider observations of iceberg-enhanced biological productivity in the northwestern Wed-
- 681

- 682 dell Sea, *Geophys. Res. Lett.*, 42, 459465.
- 683 De Rydt, J., and G. H. Gudmundsson (2016), Coupled ice shelf ocean modeling and
684 complex grounding line retreat from a seabed ridge. *J. of Geophys. Res.: Earth Surface*,
685 121(5), 865-880.
- 686 Dunne, J.P., J.G. John,, A.J. Adcroft, S.M. Griffies, R.W. Hallberg, E. Shevliakova,
687 R.J. Stouffer, W. Cooke, K.A. Dunne, M.J Harrison, and J.P. Krasting (2012), GFDL's
688 ESM2 global coupled climate-carbon Earth System Models. Part I: Physical formulation
689 and baseline simulation characteristics. *J. of Climate*, 25(19), 6646-6665.
- 690 Depoorter, M. A., J. L. Bamber, J. A. Griggs, J. T. M. Lenaerts, Stefan RM Ligtenberg,
691 M. R. van den Broek, and G. Moholdt (2013), Calving fluxes and basal melt rates of
692 Antarctic ice shelves. *Nature*, 502(7469), 89-92.
- 693 Determan J., Gerdes R. (1994), Melting and freezing beneath ice shelves: implications
694 from a three-dimensional ocean-circulation model. *Ann. Glaciol.*, 20, 413-419.
- 695 Dowdeswell, J. A., and J. L. Bamber (2007), Keel depths of modern Antarctic icebergs
696 and implications for sea-floor scouring in the geological record. *Marine Geology*, 243(1),
697 120-131.
- 698 Duprat, L. P., G. R. Bigg, and D. J. Wilton (2016), Enhanced Southern Ocean marine
699 productivity due to fertilization by giant icebergs. *Nature Geoscience*.
- 700 Eckert, E. R. G. (1950). Introduction to the Transfer of Heat and Mass. McGraw-Hill.
- 701 Gladstone, R. M., G. R. Bigg, and K. W. Nicholls. (2001), Iceberg trajectory modeling
702 and meltwater injection in the Southern Ocean (19782012). *J. of Geophys. Res.: Oceans*,
703 106(C9), 19903-19915.

- 704 Goldberg, D. N., C. M. Little, O. V. Sergienko, A. Gnanadesikan, R. Hallberg, and M.
705 Oppenheimer (2012), Investigation of land ice?ocean interaction with a fully coupled
706 ice-ocean model: 1. Model description and behavior. *J. of Geophys. Res.: Earth Surface*,
707 117(F2).
- 708 Gladish, C. V., D. M. Holland, P. R. Holland, and S. F. Price (2012), Ice-shelf basal
709 channels in a coupled ice/ocean model. *J. of Glaciol.*, 58(212), 1227-1244.
- 710 Grosfeld K., R. Gerdes, J. Determan (1997), Thermohaline circulation and interaction
711 between ice shelf cavities and the adjacent open ocean. *J. Phys. Oceanogr.*, **102**, C7,
712 15959-15610.
- 713 Grosfeld, K., and H. Sandhger, (2004). The evolution of a coupled ice shelfocean system
714 under different climate states. *Global and Planetary Change*, 42(1), 107-132.
- 715 Hallberg, R., A. Adcroft, J. P. Dunne, J. P., Krasting, R. J., and Stouffer (2013), Sensitiv-
716 ity of twenty-first-century global-mean steric sea level rise to ocean model formulation.
717 *J. of Climate*, 26(9), 2947-2956.
- 718 Holland D. M., Jenkins A. (2001), Adaptation of an isopycnic coordinate ocean model for
719 the study of circulation beneath ice shelves. *Mon. Wea. Rev.*, 129, 1905-1927.
- 720 Holland P. R. and D. L. Feltham (2006), The effects of rotation and ice shelf topography
721 on frazil-laden Ice Shelf Water plumes. *J. Phys. Oceanogr.*, 36, 2312-2327.
- 722 Holland, D. M., and A. Jenkins (1999), Modeling thermodynamic ice-ocean interactions
723 at the base of an ice shelf. *J. of Phys. Oceanogr.* 29.8, 1787-1800.
- 724 Hellmer H.H., Olbers D. J. (1989), A two-dimensional model for the thermohaline circu-
725 lation under an ice shelf. *Antarctic Science*, 1, 325- 336.

- 726 Hopkins, M. A. (1996). On the mesoscale interaction of lead ice and floes. *J. of Geophys.*
727 *Res.: Oceans*, 101(C8), 18315-18326.
- 728 Jakobsen, T. (2001). Advanced character physics. In *Game Developers Conference*, Vol.
729 3.
- 730 Jenkins, A., P. Dutrieux, S. S. Jacobs, S. D. McPhail, J. R. Perrett, A. T. Webb, and
731 D. White (2010), Observations beneath Pine Island Glacier in West Antarctica and
732 implications for its retreat. *it Nature Geo.*, 3(7), 468-472.
- 733 Jacobs, S. S., A. Jenkins, C. F. Giulivi, and P. Dutrieux (2011). Stronger ocean circulation
734 and increased melting under Pine Island Glacier ice shelf. *Nature Geo.*, 4(8), 519-523.
- 735 Jongma, J. I., E. Driesschaert, T. Fichefet, H. Goosse, and H. Renssen (2009), The effect of
736 dynamic-thermodynamic icebergs on the Southern Ocean climate in a three-dimensional
737 model, *Ocean Modell.*, 26, 104113.
- 738 Lewis E.L. and R.G. Perkin (1986), Ice pumps and their rates. *J. of Geophys. Res.*, 91,
739 11756-11762.
- 740 Losch, M. (2008). Modeling ice shelf cavities in az coordinate ocean general circulation
741 model. *J. of Geophys. Res.: Oceans*, 113(C8).
- 742 Li, B., H. Li, Y. Liu, A. Wang and S. Ji (2014), A modified discrete element model for
743 sea ice dynamics. *Acta Oceanologica Sinica*, 33(1), 56-63.
- 744 Liu, M. B. and G. R. Liu (2010), Smoothed particle hydrodynamics (SPH): an overview
745 and recent developments. *Archives of computational methods in engineering*, 17(1), 25-
746 76.
- 747 Lichy, C., and H. H. Hellmer (2001). Modeling giant-iceberg drift under the influence of
748 sea ice in the Weddell Sea, Antarctica. *J. of Glaciol.*, 47(158), 452-460.

- 749 Levermann, A., T. Albrecht, R. Winkelmann, M. A. Martin, M. Haseloff, and I. Joughin.
750 (2012), Kinematic first-order calving law implies potential for abrupt ice-shelf retreat.
751 *The Cryosphere*, 6(2), 273-286.
- 752 Martin, T., and Adcroft, A. (2010), Parameterizing the fresh-water flux from land ice
753 to ocean with interactive icebergs in a coupled climate model. *Ocean Modelling*, 34(3),
754 111-124.
- 755 Marsh, R., V. O. Ivchenko, N. Skliris, S. Alderson, G. R. Bigg, G. Madec, A. T. Blaker
756 Y. Aksenov, B. Sinha, A.C. Coward, and J.L. Sommer (2015), NEMOICB (v1. 0):
757 interactive icebergs in the NEMO ocean model globally configured at eddy-permitting
758 resolution. *Geoscientific Model Development* 8, no. 5 (2015): 1547-1562.
- 759 MacAyeal D.R. (1984), Thermohaline Circulation Below the Ross Ice Shelf: A Conse-
760 quence of Tidally Induced Vertical Mixing and Basal Melting. *J. Geophys. Res.*, 89,
761 597-606
- 762 Nicholls K.W. (1996), Temperature variability beneath Ronne Ice Shelf, Antarctica, from
763 thermistor cables. *J. Phys. Oceanogr.*, 11, 1199-1210.
- 764 Nicholls KW, Østerhus S, Makinson K (2009), Ice-Ocean processes over the continental
765 shelf of the southern Weddell Sea, Antarctica: a review. *Rev. Geophys.* 47(3).
- 766 Omelyan, I. P., M. I. Mryglod, and R. Folk (2002), Optimized Verlet-like algorithms for
767 molecular dynamics simulations. *Physical Review E*, 65(5), 056706.
- 768 Rignot, E., S. Jacobs, J. Mouginot, and B. Scheuchl (2013), Ice-shelf melting around
769 Antarctica. *Science*, 341, no. 6143 (2013): 266-270.
- 770 Robinson, N. J., M. J. M. Williams, P. J. Barrett, and A. R. Pyne (2010), Observations of
771 flow and ice-ocean interaction beneath the McMurdo Ice Shelf, Antarctica, *J. Geophys.*

- 772 Res., 115, C03025
- 773 Pan, W., A. M. Tartakovsky, and J. J. Monaghan (2013). Smoothed particle hydrody-
774 namics non-Newtonian model for ice-sheet and ice-shelf dynamics. *J. of Comp. Phys.*,
775 242, 828-842.
- 776 Pralong, A., and M. Funk (2005), Dynamic damage model of crevasse opening and appli-
777 cation to glacier calving, *J. Geophys. Res.*, 110, B01309.
- 778 Sergienko, O. V. (2013). Basal channels on ice shelves. *J. of Geophys. Res.: Earth Surface*,
779 118(3), 1342-1355.
- 780 Silva, T. A. M., Bigg, G. R., and Nicholls, K. W. (2006), Contribution of giant icebergs
781 to the Southern Ocean freshwater flux. *J. of Geophys. Res.: Oceans*, 111(C3).
- 782 Smith, K., B. Robison, J. Helly, R. Kaufmann, H. Ruhl, H., T. Shaw, and M. Vernet
783 (2007), Free-drifting icebergs: Hotspots of chemical and biological enrichment in the
784 Weddell Sea, *Science*, 317, 478482.
- 785 Stern, A. A., D. M. Holland, P. R. Holland, A. Jenkins and J. Sommeria (2014), The effect
786 of geometry on ice shelf ocean cavity ventilation: a laboratory experiment. *Experiments*
787 in Fluids, 55(5), 1-19.
- 788 Stern, A.A., Johnson, E., Holland, D.M., Wagner, T.J., Wadhams, P., Bates, R., Abra-
789 hamsen, E.P., Nicholls, K.W., Crawford, A., Gagnon, J. and Tremblay, J.E. (2015),
790 Wind-driven upwelling around grounded tabular icebergs. *J. of Geophys. Res.: Oceans*,
791 120(8), 5820-5835.
- 792 Stern, A. A., A. Adcroft, and O. Sergienko (2016), The effects of Antarctic iceberg calv-
793 ing?size distribution in a global climate model. *J. of Geophys. Res.: Oceans*, 121(8),
794 5773-5788.

- 795 Swope, W. C., H. C. Andersen, P. H. Berens, and K. R. Wilson (1982), A computer
796 simulation method for the calculation of equilibrium constants for the formation of
797 physical clusters of molecules: Application to small water clusters. *The Journal of*
798 *Chemical Physics* 76, no. 1, 637-649.
- 799 Tournadre, J., N. Bouvier, F. Girard-Ardhuin, and F. Remy (2016), Antarctic icebergs
800 distributions 1992-2014. *J. Geophys Res: Oceans*.
- 801 Vernet, M., et al. (2012), Islands of ice: Influence of free-drifting Antarctic icebergs on
802 pelagic marine ecosystems, *Oceanography*, 25(3), 3839
- 803 Weeks, W. F., and W. J. Campbell (1973). Icebergs as a fresh-water source: an appraisal.
804 *J. of Glaciol.*, 12(65), 207-233.
- 805 White, L., A. Adcroft, and R. Hallberg (2009), High-order regriddingremapping schemes
806 for continuous isopycnal and generalized coordinates in ocean models. *J. of Comp.*
807 *Phys.*, 228(23), 8665-8692.

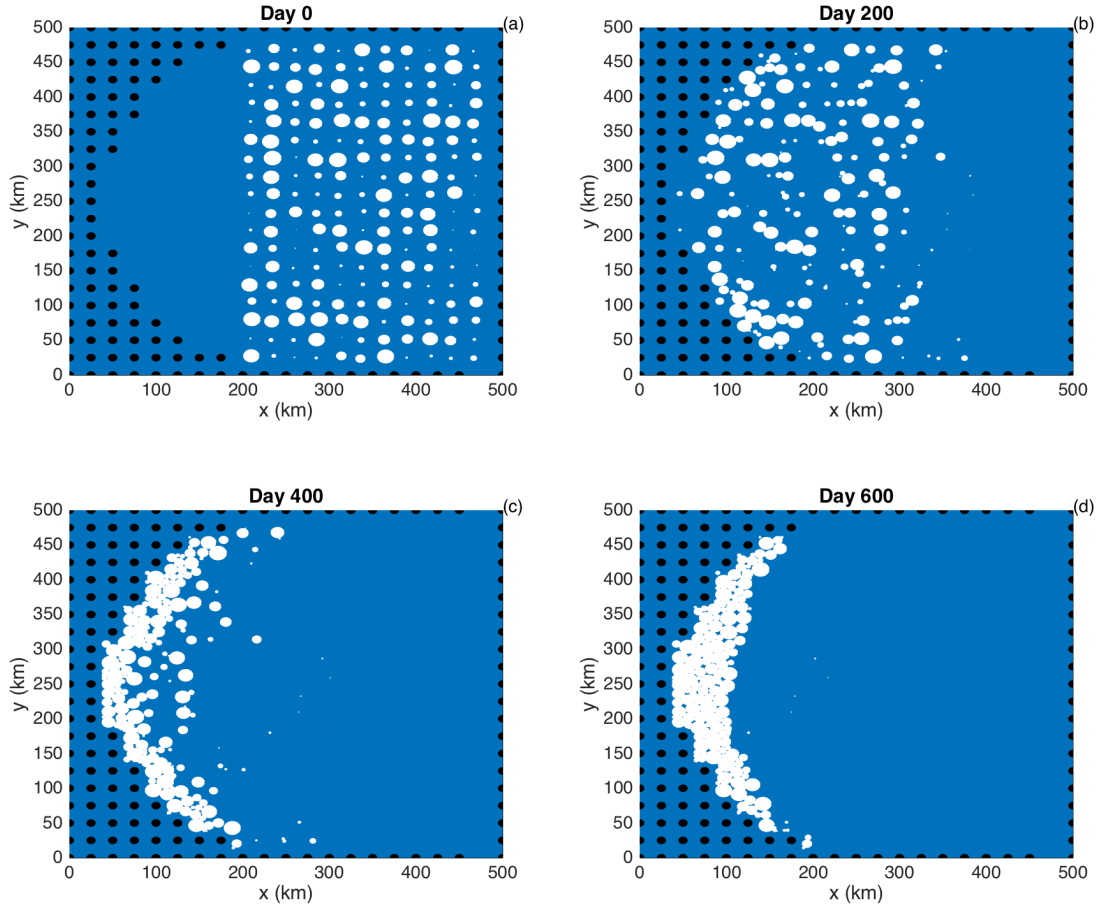


Figure 1. Results of an ice-only LIISM simulation with no bonds between ice elements. Ice elements are initialized throughout the domain, as shown in panel (a). The elements are forced by an imposed westward ocean current of $u=0.1\text{m/s}$ (no ocean model is used). Forces due to sea surface slope, atmospheric drag, Coriolis and sea ice drag are set to zero. The figure shows snapshots of ice element positions at time (a) $t=0$, (b) 200, (c) 400, (d) 600 days. The size of the dots shows the surface area (and interaction diameter) of each ice element. Land points are shown by black circles.

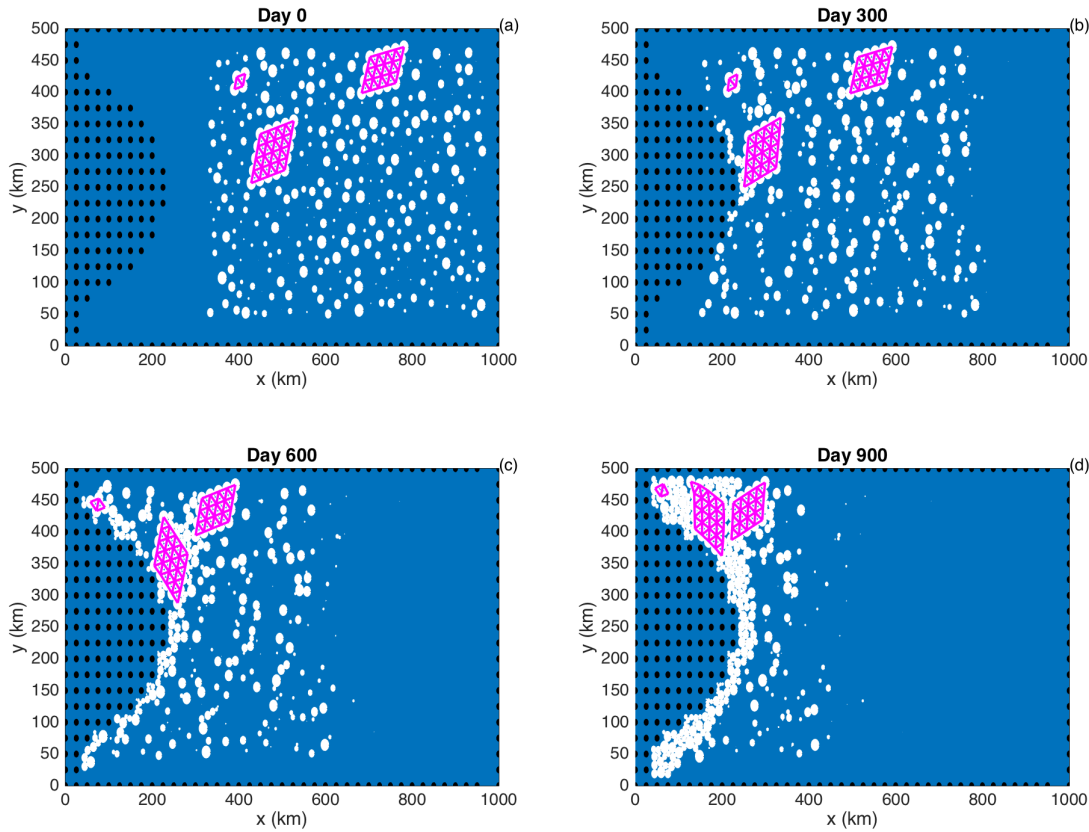


Figure 2. Results of an ice-only LIISM simulation using bonds between elements. Ice elements are initialized throughout the domain, as shown in panel (a). Three tabular icebergs are included, with 25, 16 and 4 elements respectively. The elements are forced by an imposed westward ocean current of $u=0.1\text{m/s}$ (no ocean model is used). Forces due to sea surface slope, atmospheric drag, Coriolis and sea ice drag are set to zero. The figure shows snapshots of ice element positions at time (a) $t=0$, (b) 300, (c) 600, (d) 900 days. The size of the dots shows the surface area (and interaction diameter) of each ice element. Bonds between ice elements are plotted in magenta. Land points are shown by black circles.

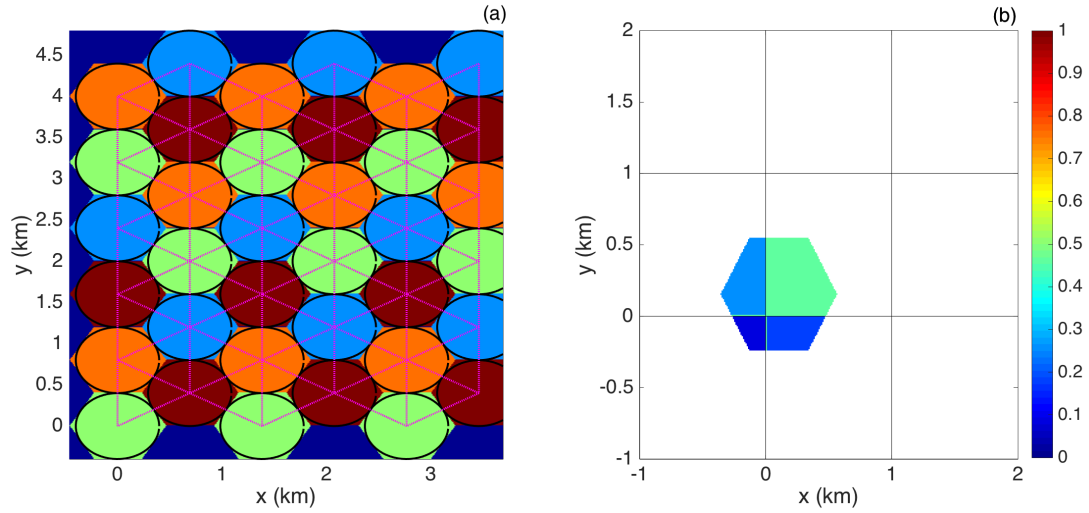


Figure 3. (a) Hexagonal elements are initialized in a staggered lattice as shown. Adjacent elements are bonded together. The centers of bonded elements are plotted in pink. The element bonds form equilateral triangles which give the larger structure rigidity. The black circles show to the interactive length scales used in element interactions. (b) Intersection of a hexagonal element and an ocean grid. The colors indicate the fraction of the hexagon that lies in each grid cell. These fractions are used as weights to spread LIISM properties to the ocean grid (see text for more details).

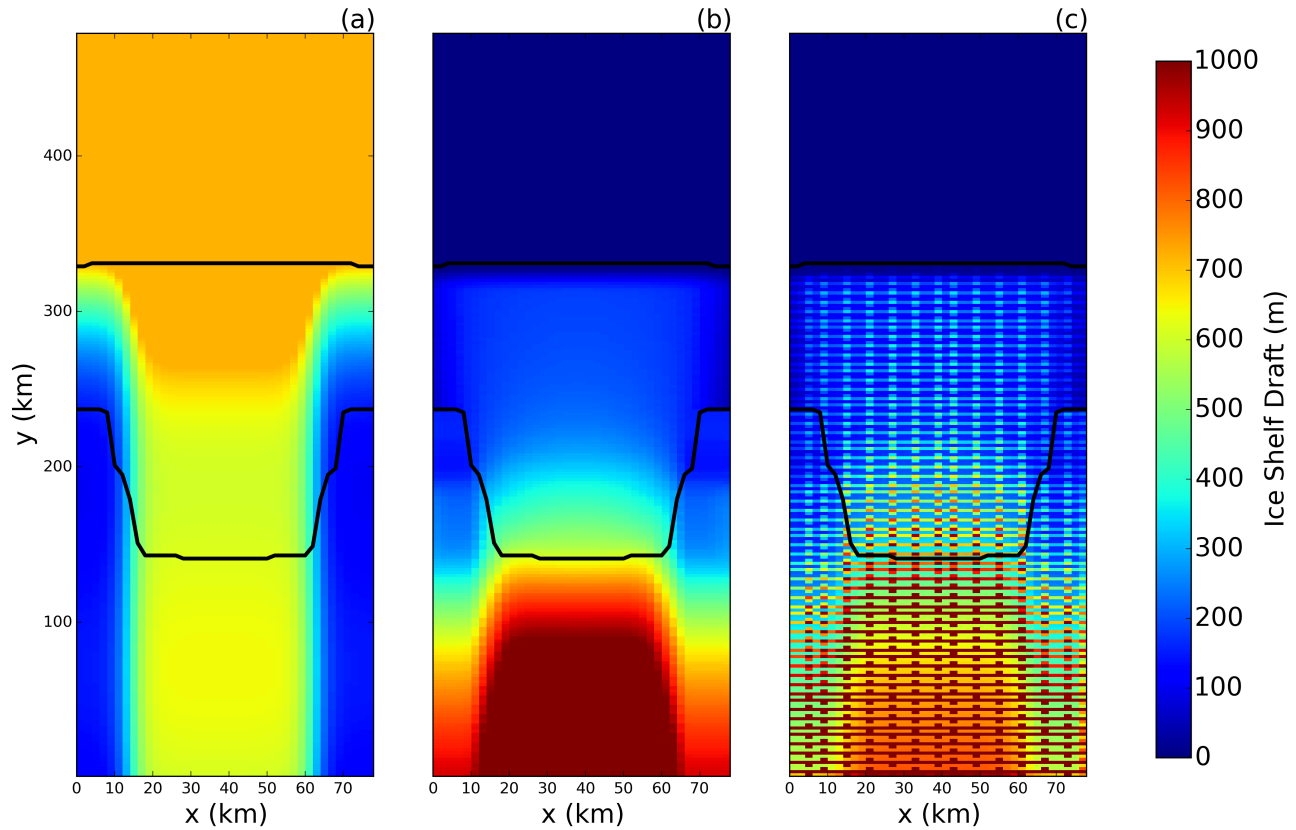


Figure 4. (a) Ocean bottom topography in MISOMIP configuration. (b) ice-shelf draft used in static shelf experiment. The ice draft is calculated from the ice mass in an ocean grid cell, which is found by spreading ice mass across ocean cells accounting for the size of each element (as explained in Section 2.3). (c) Same as in panel (b), except that the interpolation does not account for iceberg size, and instead treats elements as point masses.

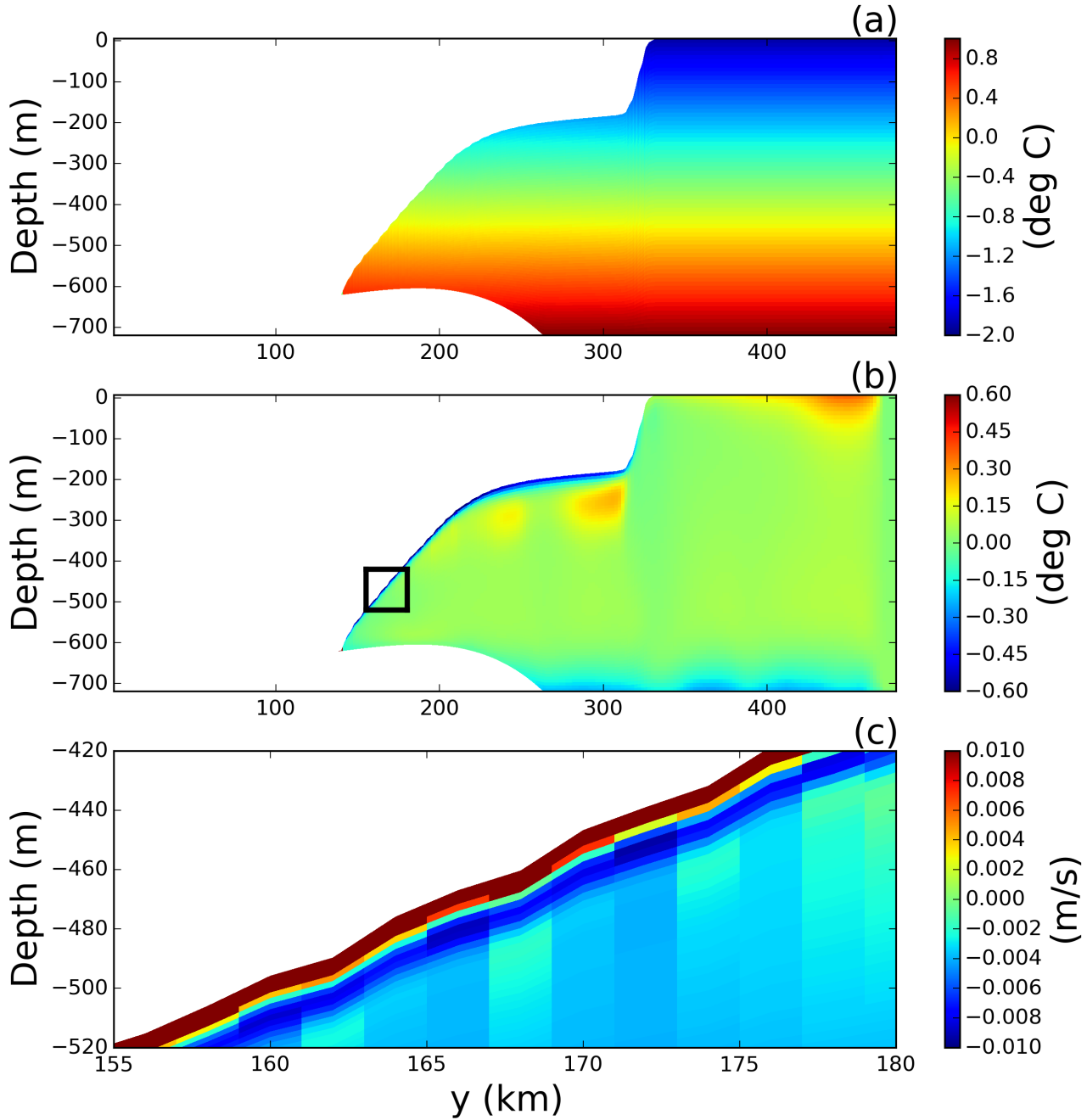


Figure 5. Results of the static ice-shelf experiment using the LIISM model coupled to MOM6.

Panels show cross sections of the (a) initial temperature field, (b) temperature anomaly after 5-years (relative to the initial field), and (c) meridional velocity near the ice-shelf base after 5 years of simulation. The region shown in panel (c) is indicated by the black box on panel (b),

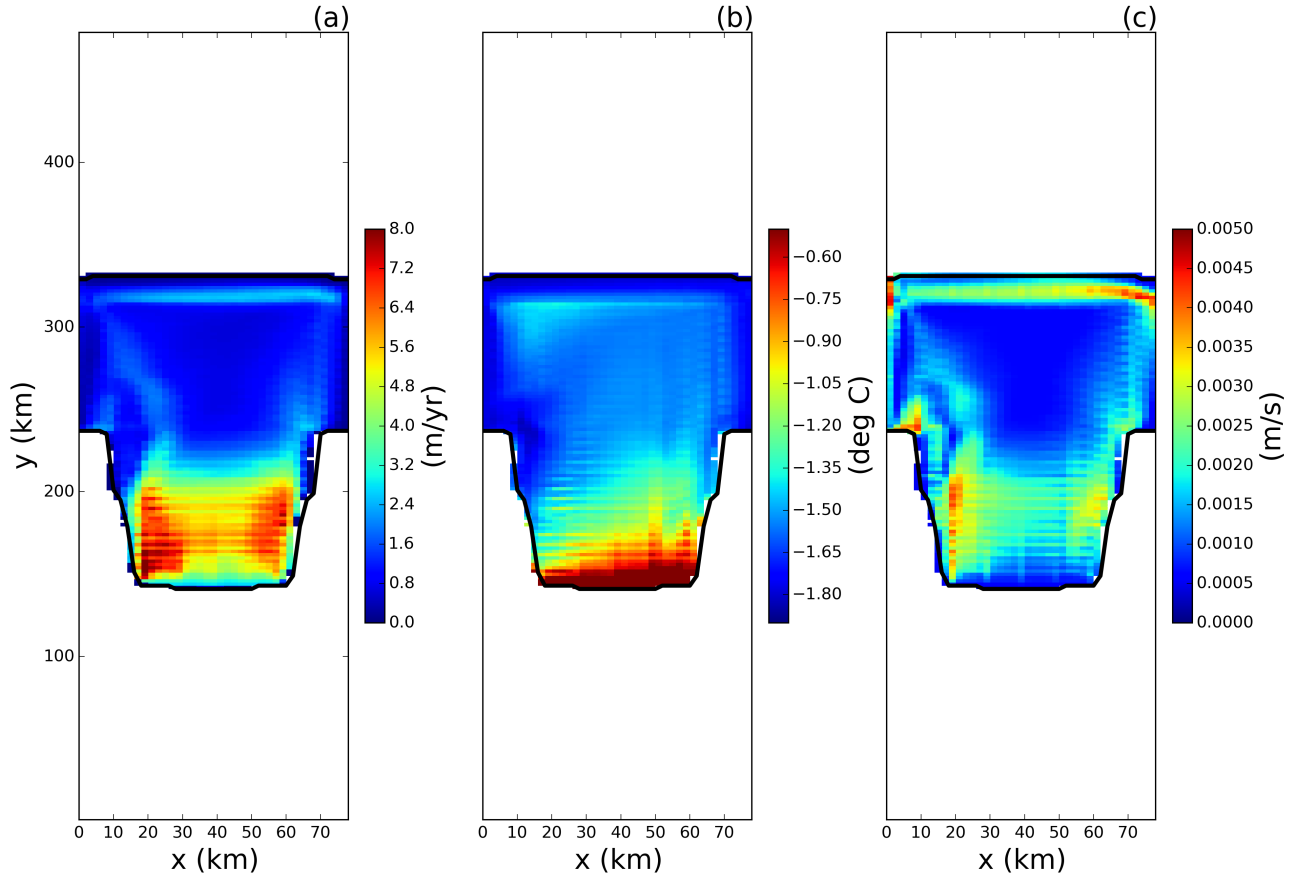


Figure 6. Results of the static ice-shelf experiment using the LIISM model coupled to MOM6.

The three panels show 5 year time average of the (a) melt rate, (b) top-of-ocean and (c) frictional velocity, u^* , at the base of the ice shelf. Fields are only shown in regions where the ice area fraction is ≥ 0.8 .

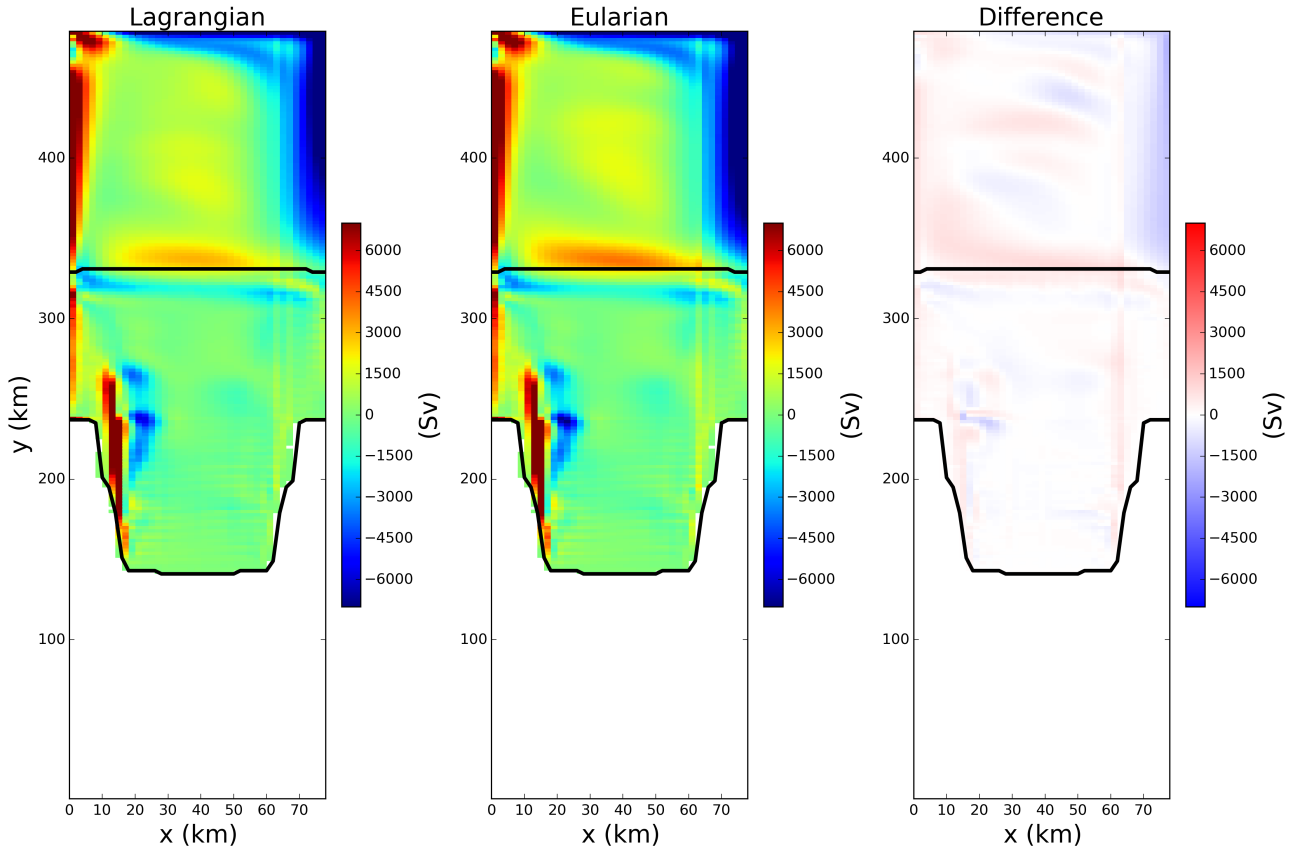


Figure 7. Time-averaged barotropic stream function in the (a) Lagrangian and (b) Eulerian simulations in the static ice-shelf configuration. Panel (c) shows the difference between panels (a) and (b). The time averages are taken over 5 years of model time, beginning at the end of the 5 year spin up period.

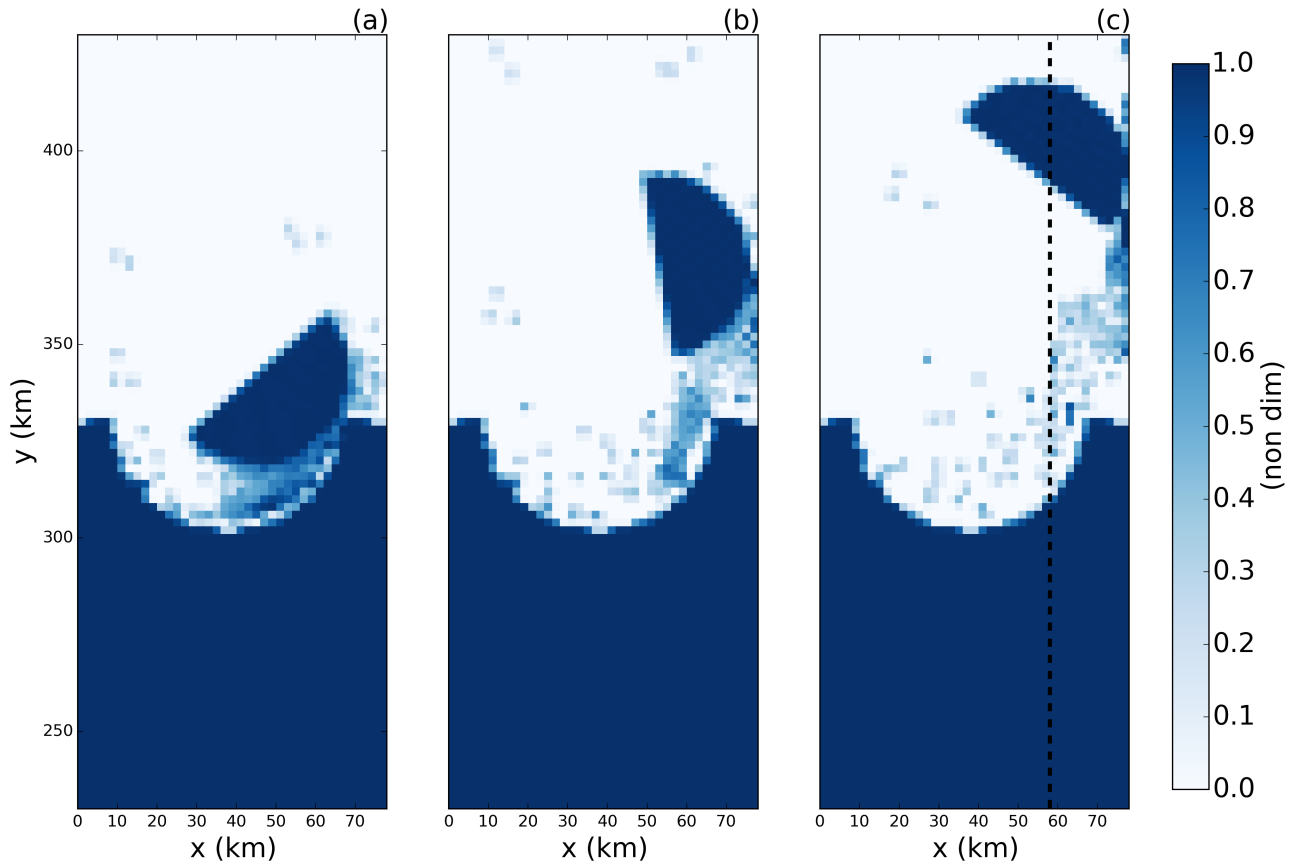


Figure 8. Snapshots of the fraction of ice cover in the LIISM tabular iceberg calving experiment. Snapshots are taken (a) 7, (b) 15, and (c) 30 days after calving. The dashed line in panel (c) shows the location of the vertical transects shown in Figures 9 and 11.

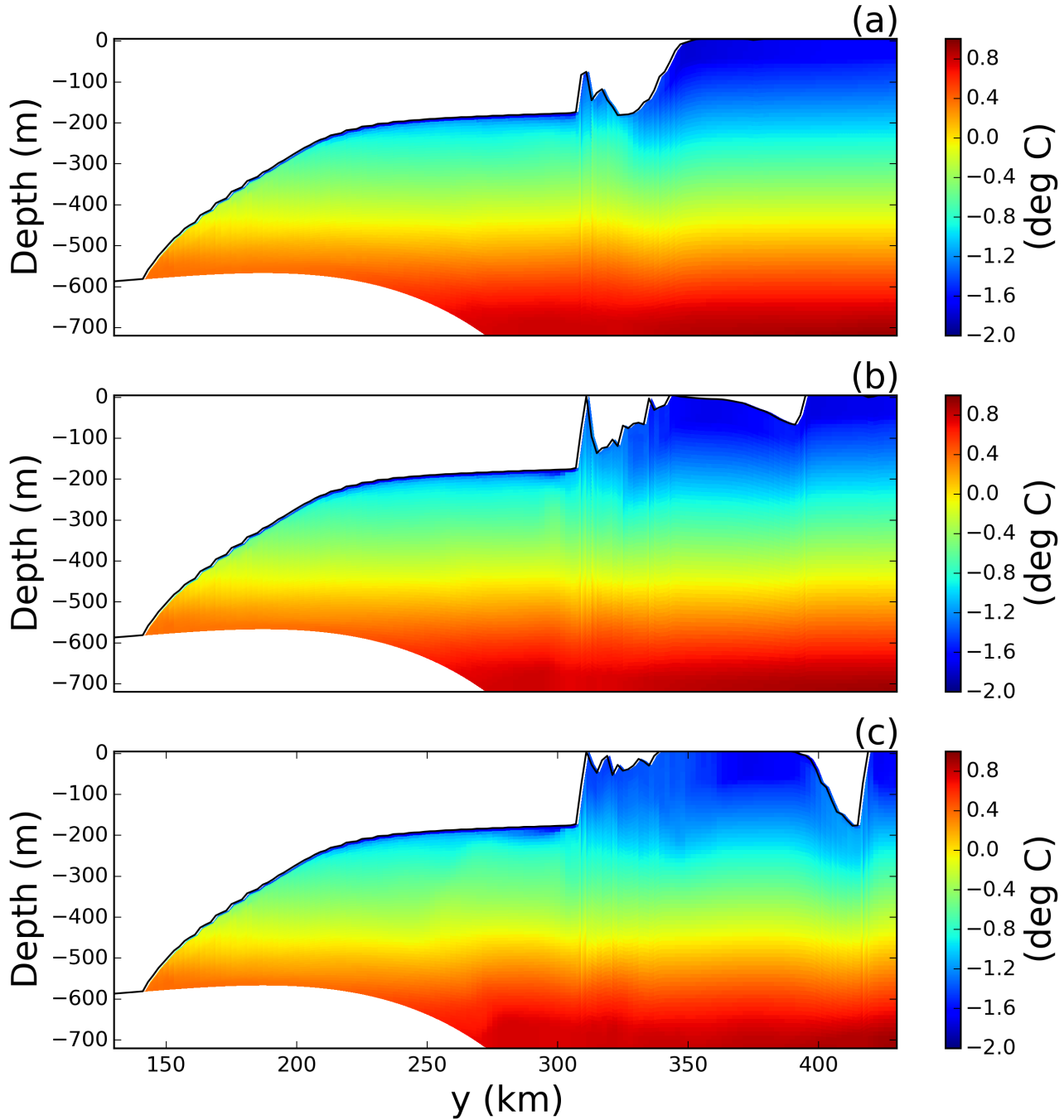


Figure 9. Snapshots of vertical sections of ocean temperature at $x = 58\text{ km}$ in the LIISM tabular iceberg calving experiment. Snapshots are taken (a) 7, (b) 15, and (c) 30 days after calving. The position of the vertical transects is shown by the dashed lines in Figure ??c.

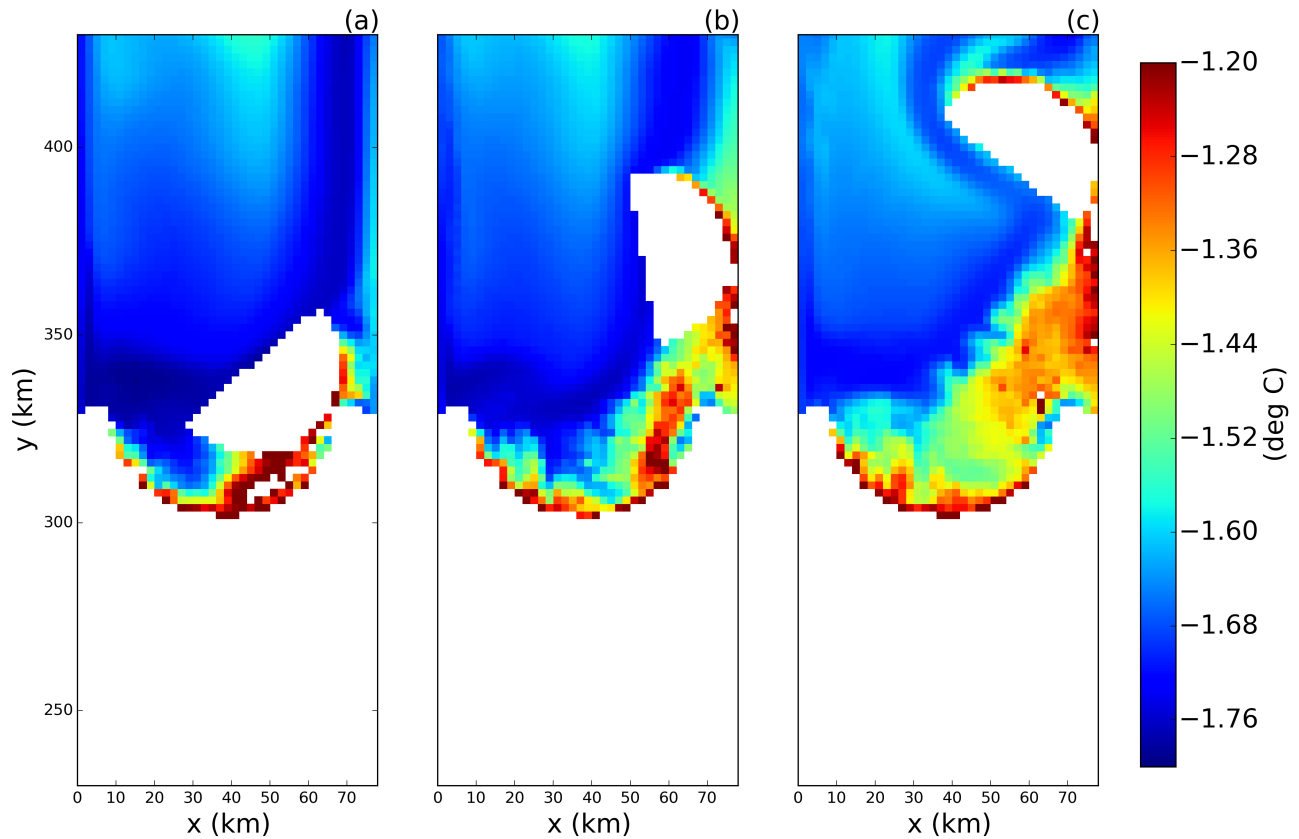


Figure 10. Snapshots of the sea surface temperature in the LIISM tabular iceberg calving experiment. Snapshots are taken (a) 7, (b) 15, and (c) 30 days after calving. Regions with ice area fraction = 1 area plotted in white.

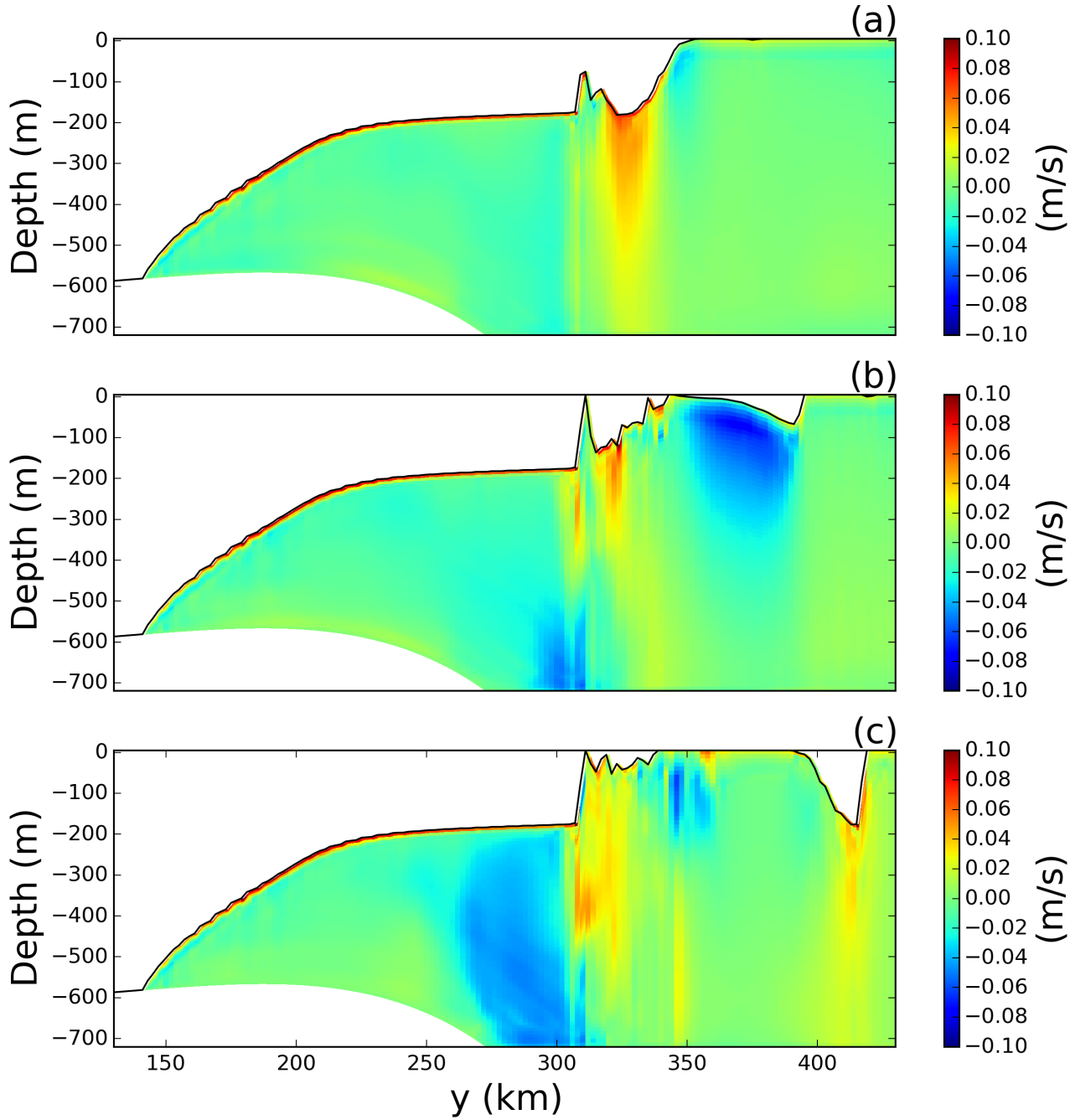


Figure 11. Snapshots of vertical sections of meridional velocity at $x = 58\text{ km}$ in the LIISM tabular iceberg calving experiment. Snapshots are taken (a) 7, (b) 15, and (c) 30 days after calving. The position of the transects is shown by the dashed line in Figure 8c.

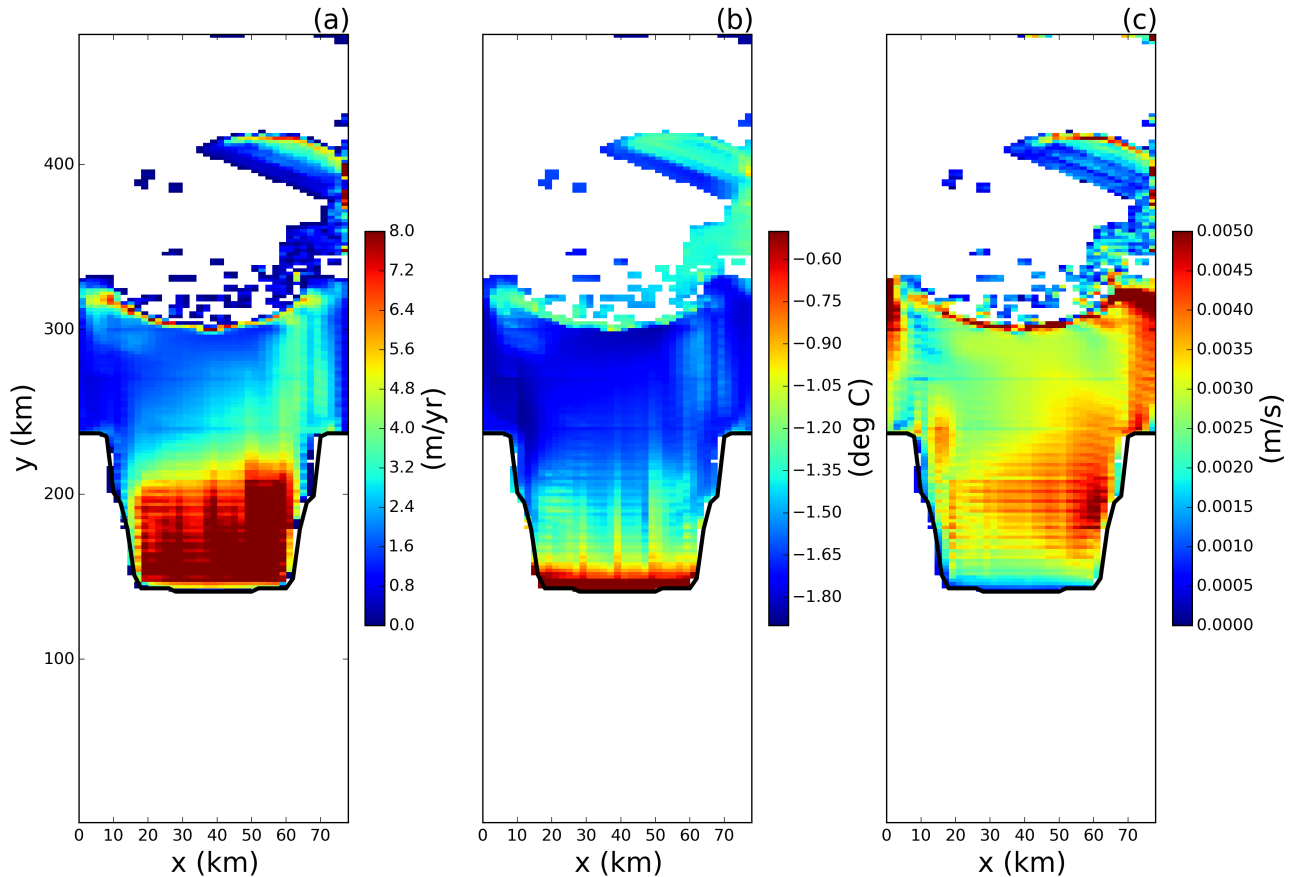


Figure 12. Results of the tabular iceberg calving simulation 30 days after the iceberg calves.

The three panels show snapshots of the (a) melt rate, (b) top-of-ocean temperature and (c) u^* at the base of the ice shelf. Fields are only shown in regions where the ice area fraction is ≥ 0.8 .

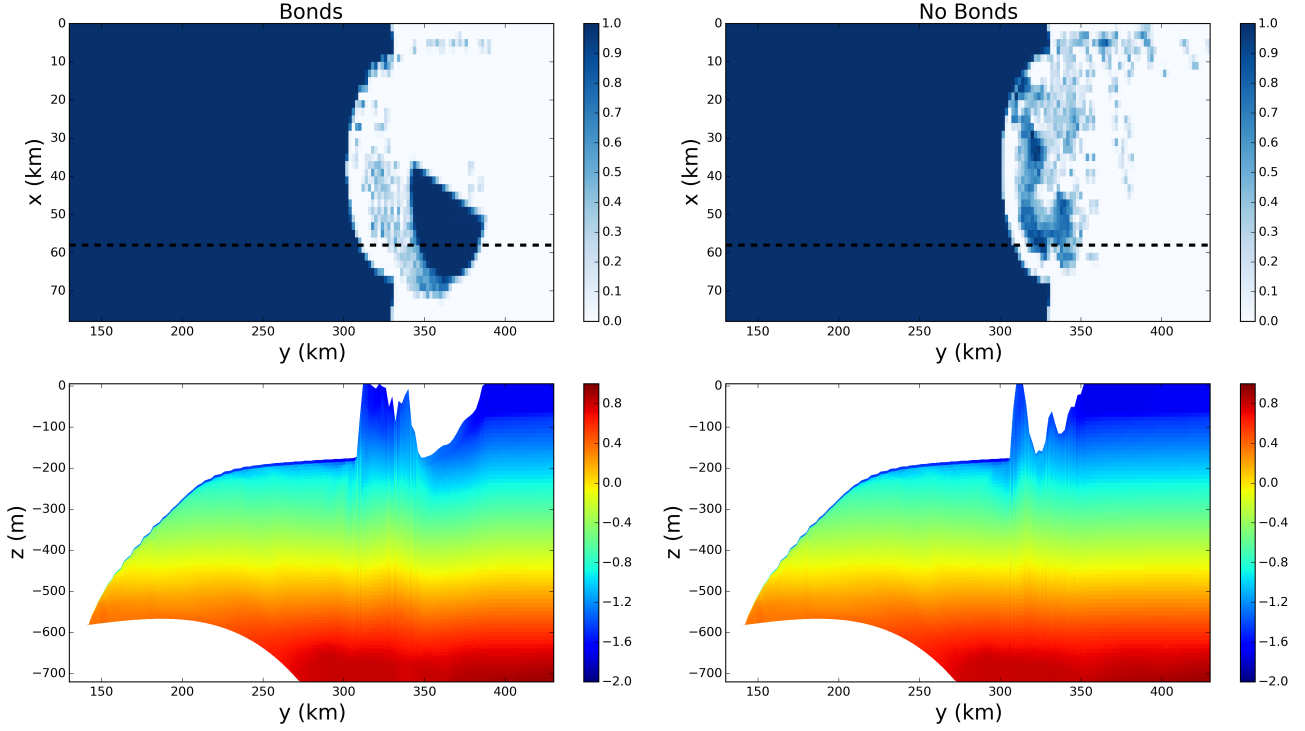


Figure 13. Results from the tabular iceberg calving experiment with and without iceberg bonds. The top row shows the fractional ice cover for the simulations (a) with and (b) without numerical bonds. The bottom row shows the corresponding vertical temperature section at $x = 58\text{ km}$ for the simulation (c) with and (d) without bonds. The location of the vertical transects in panels (c) and (d) are shown by the dashed lines in panels (a) and (b), respectively. All snapshots are taken at time $t = 30$ days. The simulations uses wind stress $\vec{\tau} = \langle 0.0, 0.05 \rangle$.

Parameter	Symbol	Value	Unit
Domain Length	L_x	80	km
Domain Width	L_y	480	km
Horizontal Resolution	Δx	2	km
Number of vertical layers	N_l	72	non-dim
Horizontal Viscosity	ν_H	6.0	$\frac{m^2}{s}$
Diapycnal Viscosity	ν_V	10^{-3}	$\frac{m^2}{s}$
Horizontal Diffusivity	ϵ_H	1.0	$\frac{m^2}{s}$
Diapycnal Diffusivity	ϵ_V	5×10^{-5}	$\frac{m^2}{s}$
Initial Surface Temperature	T_t	-1.9	$^{\circ}C$
Initial Bottom Temperature	T_b	1.0	$^{\circ}C$
Initial Surface Salinity	S_t	33.8	psu
Initial Bottom Salinity	S_b	34.7	psu
Maximum Ocean depth	H_{ocean}	720	m
Relaxation Time of Sponge Layer	T_{sponge}	0.1	days
Time Step for Static Shelf Experiment	dt_{Static}	1000	s
Time Step for Iceberg Calving Experiment	$dt_{Calving}$	10	s

10. Supplementary Figures

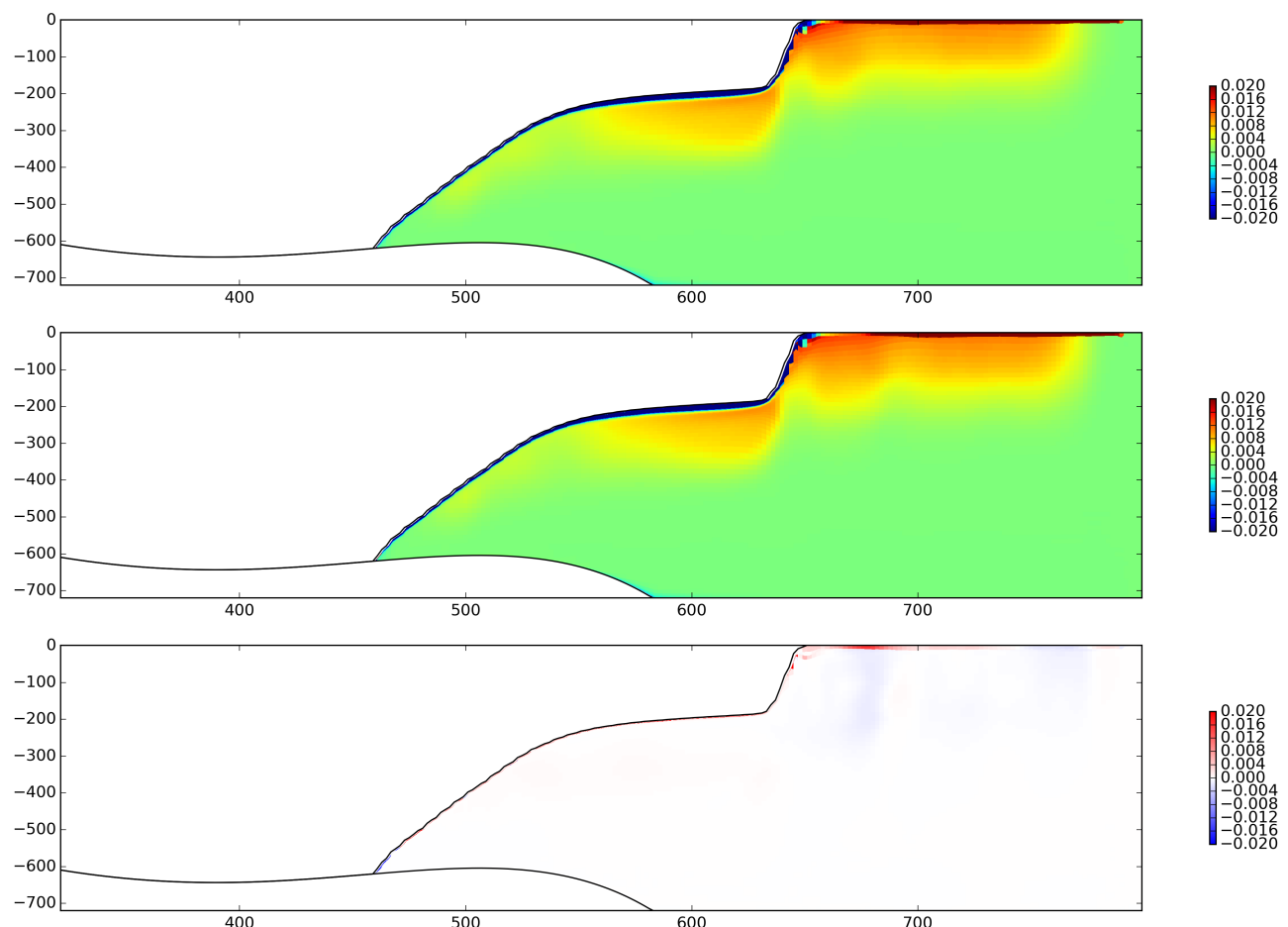


Figure S1. Comparison of Eulerian ice-shelf model and Lagrangian ice-shelf model salinity fields.

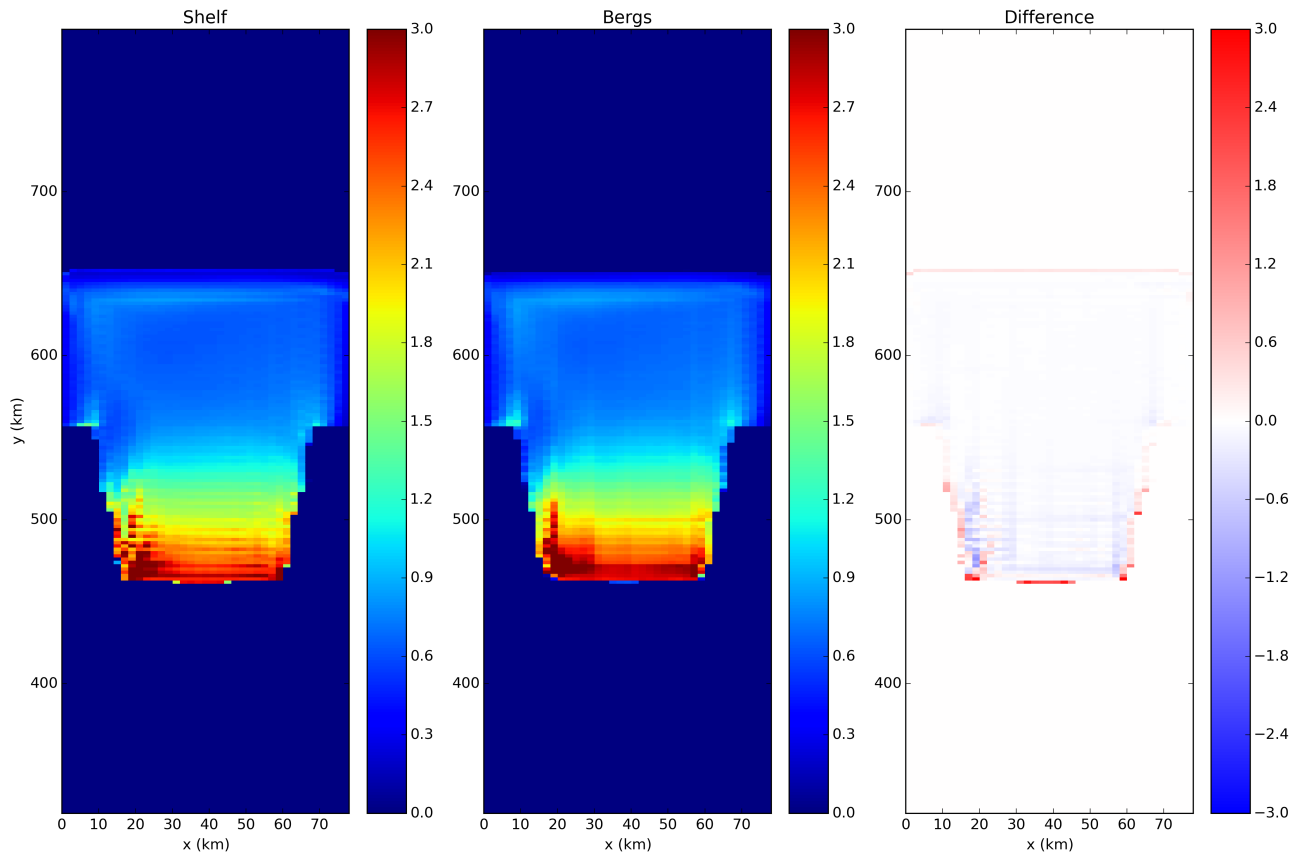


Figure S2. Comparison of Eulerian ice-shelf model and Lagrangian Ice shelf model melt fields.

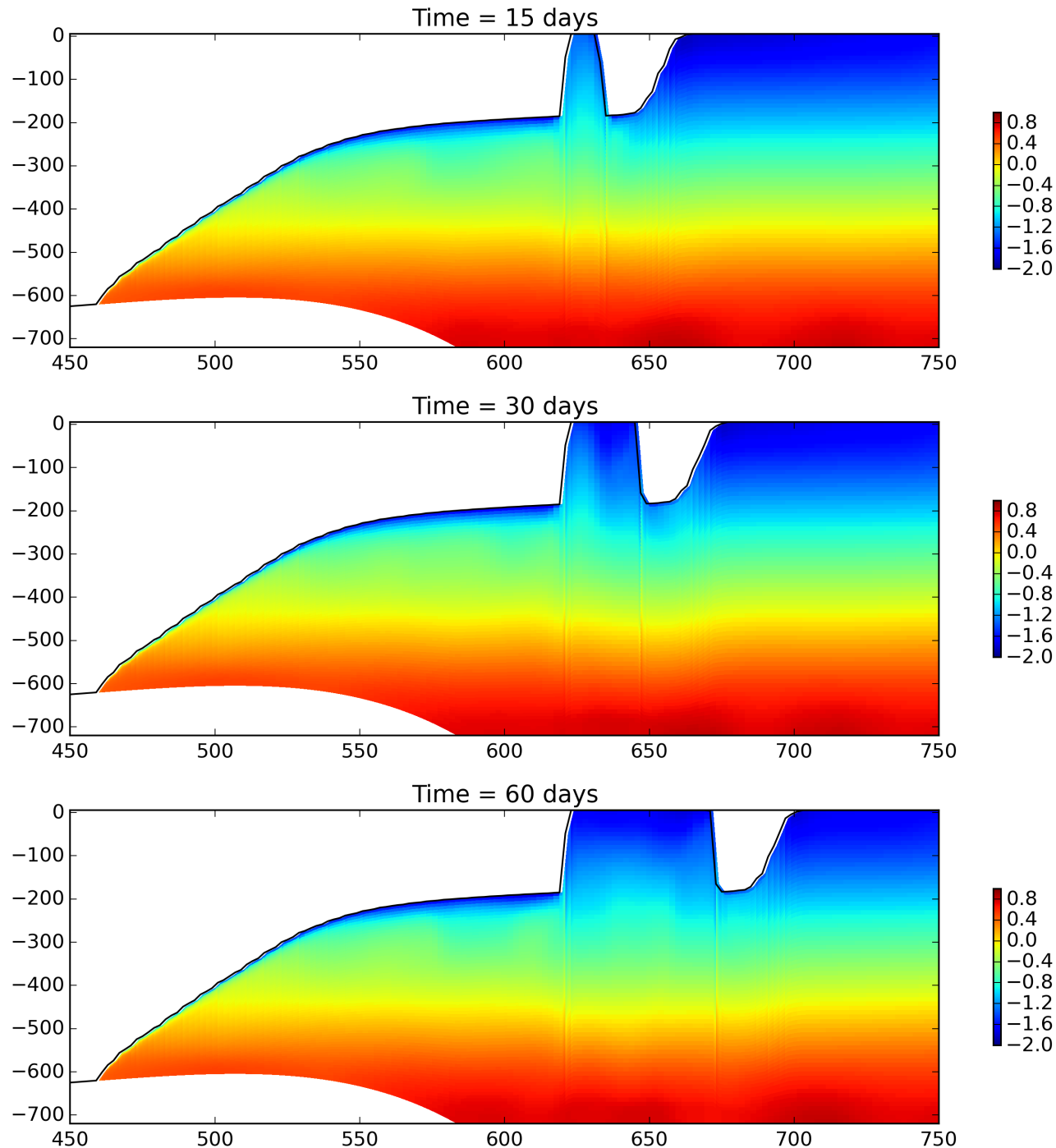


Figure S3. Layer: Temperature section at $y = \frac{L_y}{2}$ for the tabular iceberg calving with fixed velocity simulation (using the LIISM ice shelf) at time (a) $t=15$, (b) $t=30$, and (c) $t=60$ days.

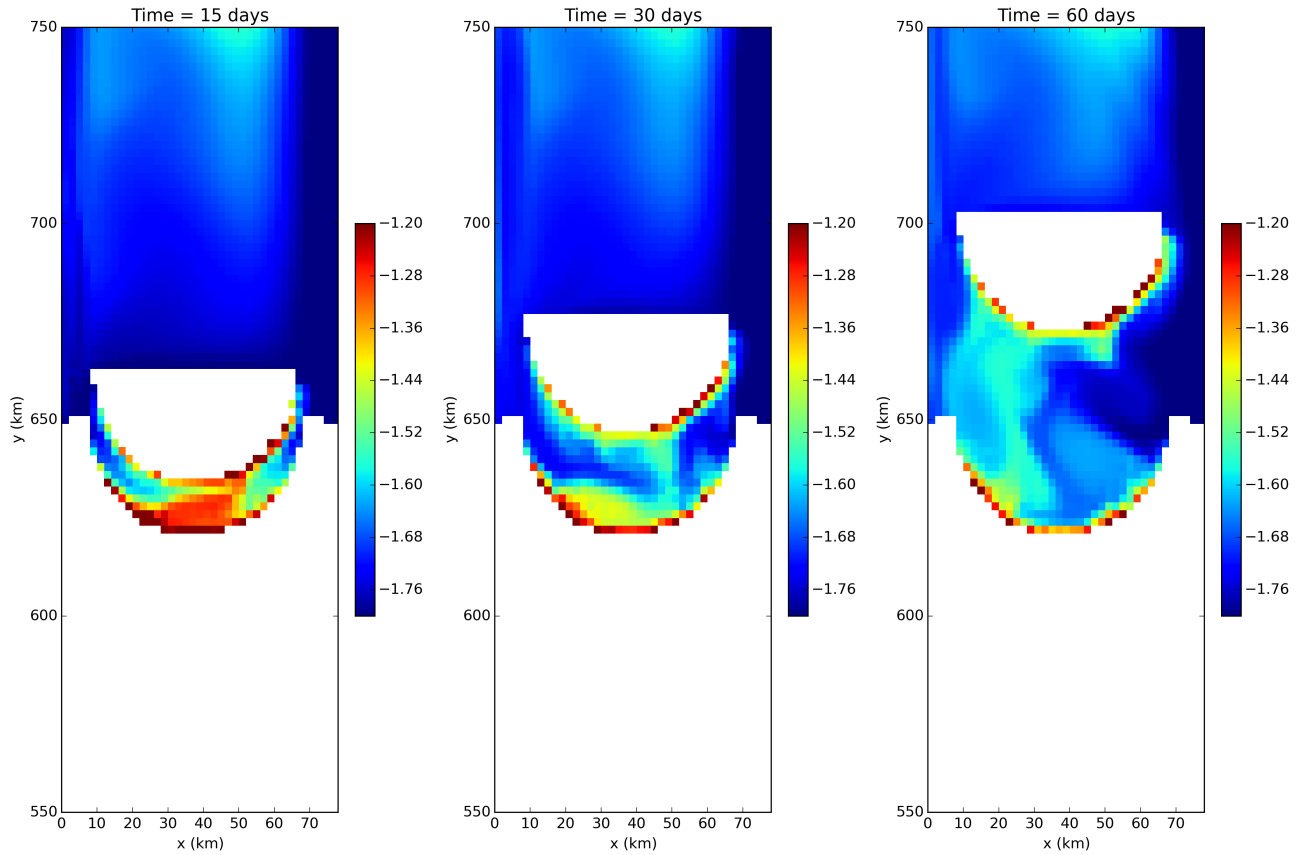


Figure S4. Layer: Sea surface temperature for the tabular iceberg calving with fixed velocity simulation at time (a) $t=15$, (b) $t=30$, and (c) $t=60$ days.

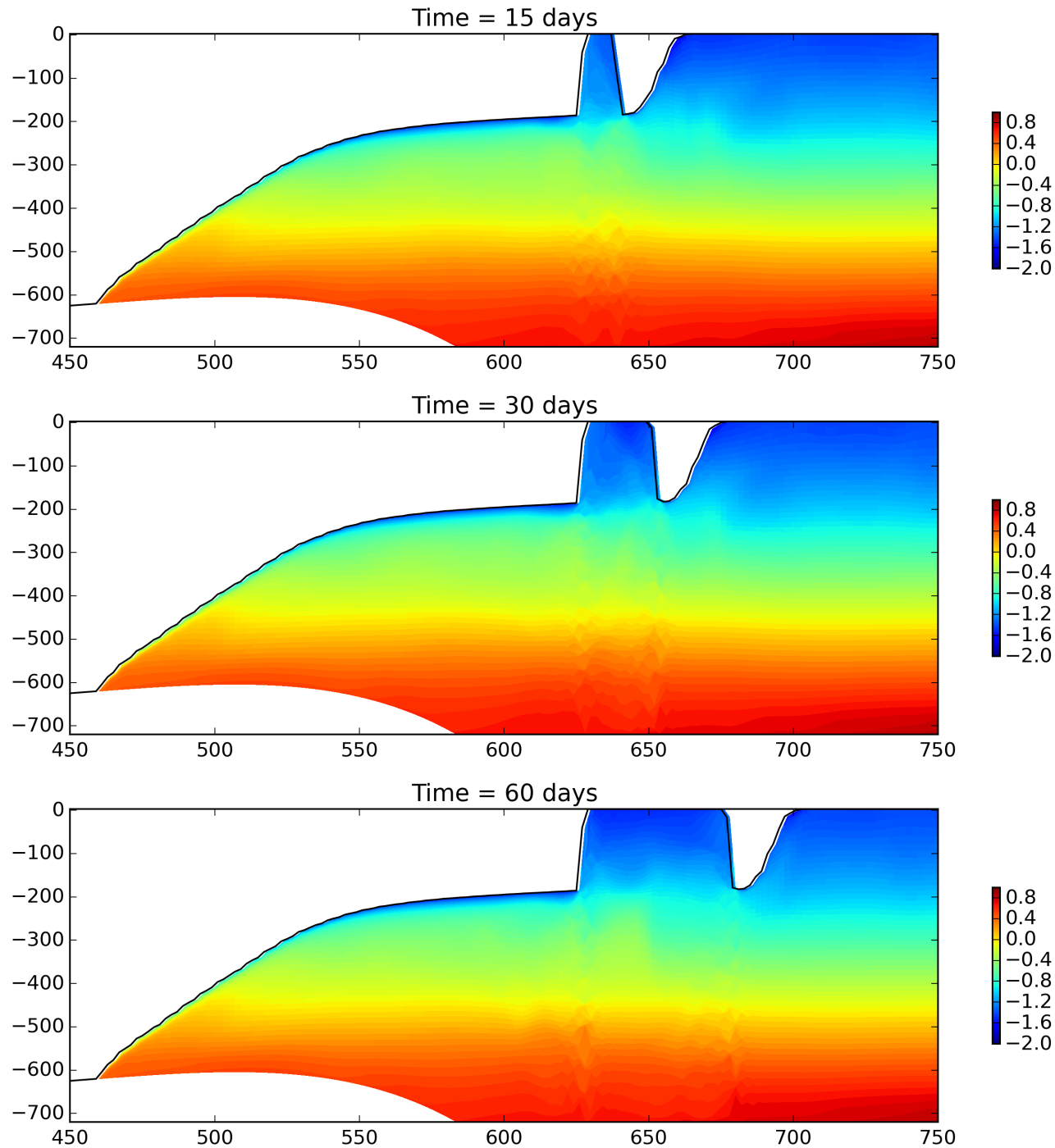


Figure S5. Layer: Temperature section at $y = \frac{L_y}{2}$ for the tabular iceberg calving with fixed velocity simulation (using the LIISM ice shelf) at time (a) $t=15$, (b) $t=30$, and (c) $t=60$ days.

11. Layer versions

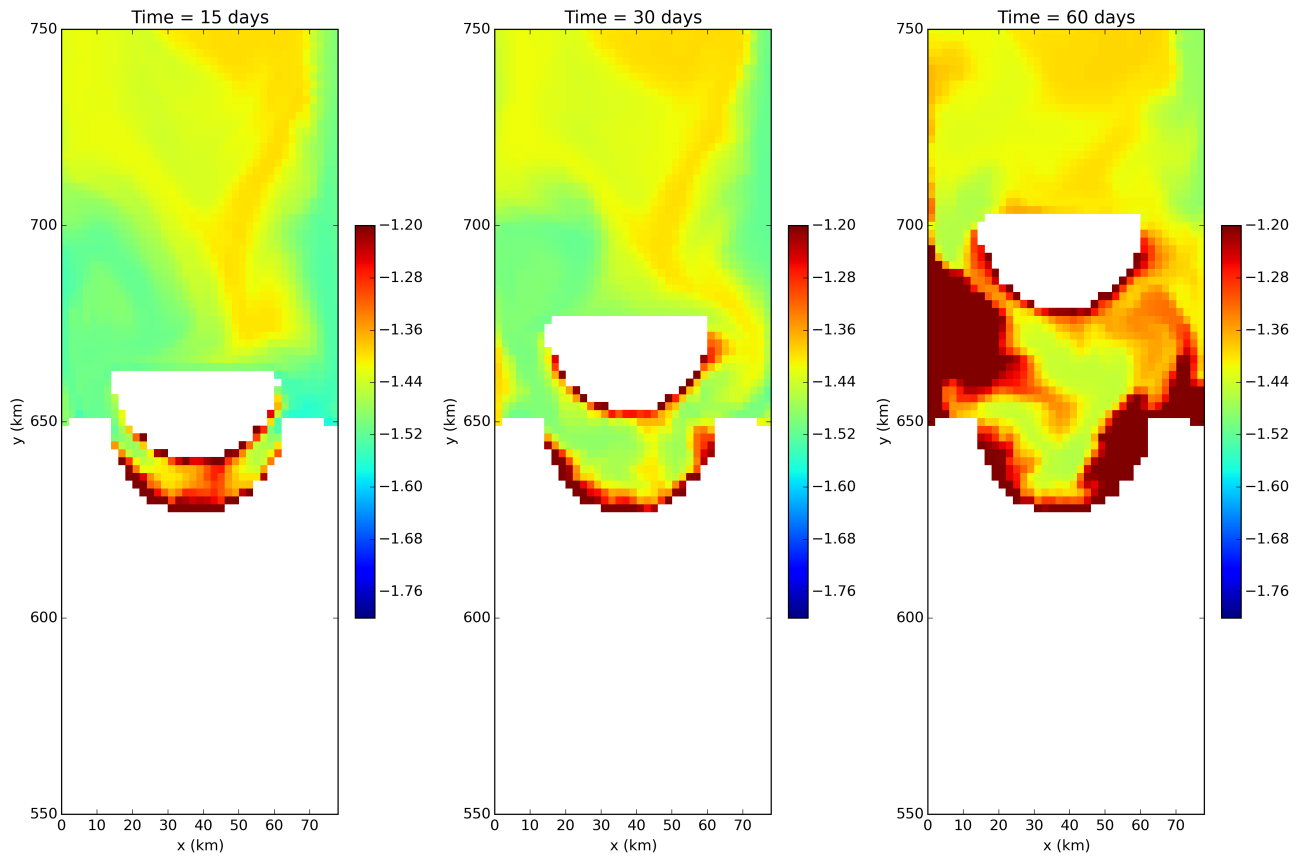


Figure S6. Layer: Sea surface temperature for the tabular iceberg calving with fixed velocity simulation at time (a) $t=15$, (b) $t=30$, and (c) $t=60$ days.

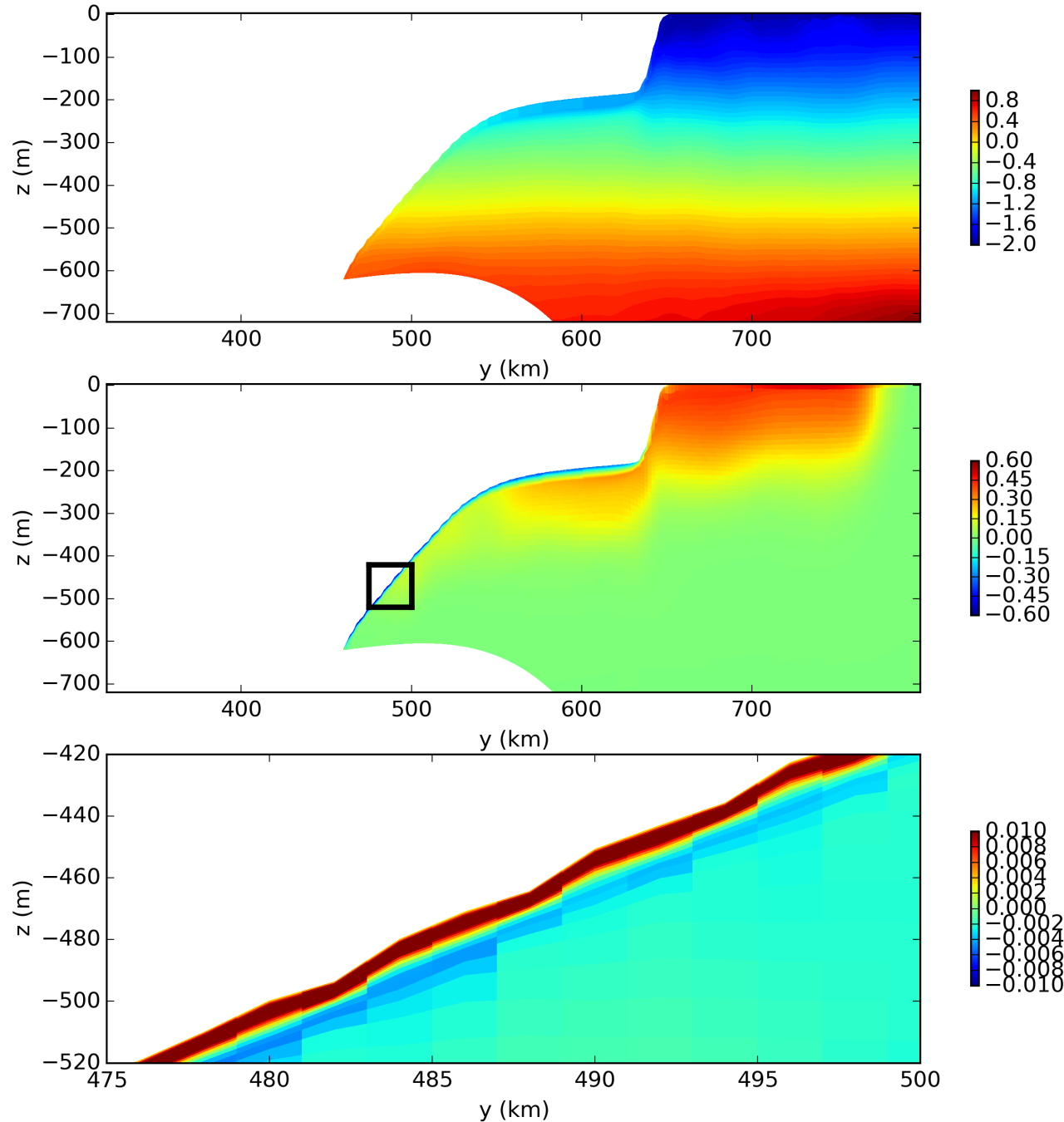


Figure S7. Layered: Results of the static ice-shelf experiment using the LIISM model. Panels show snapshots of cross sections of the (a) temperature field after 1 time step, (b) temperature anomaly after 5-years (relative the the initial field), and (c) meridional velocity after 5 years.

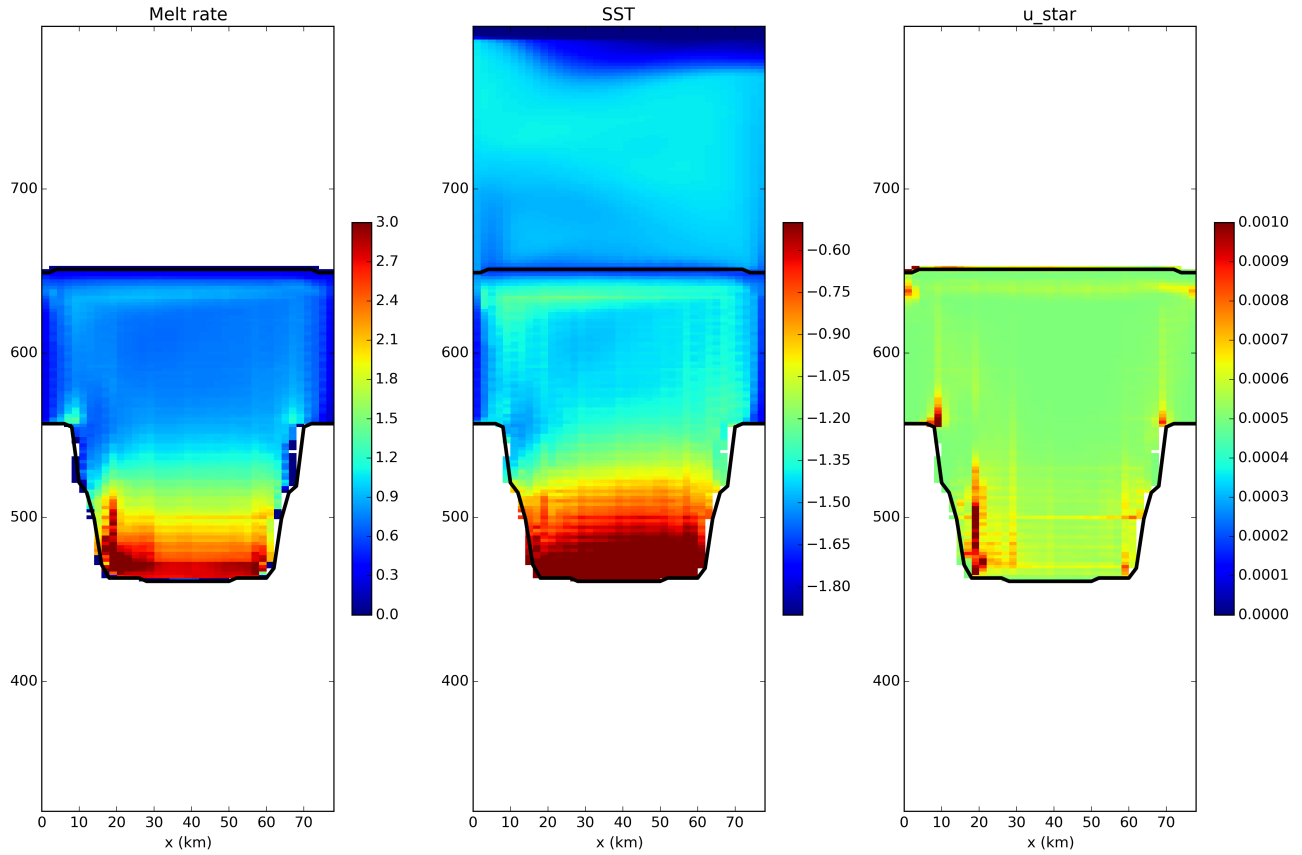


Figure S8. Layer: Results of the static ice-shelf experiment using the LIISM model. The three panels show 5 year time average of the (a) melt rate, (b) ocean surface temperature and (c) u^* in the top layer of the simulation (at the surface or directly below the ice shelf).

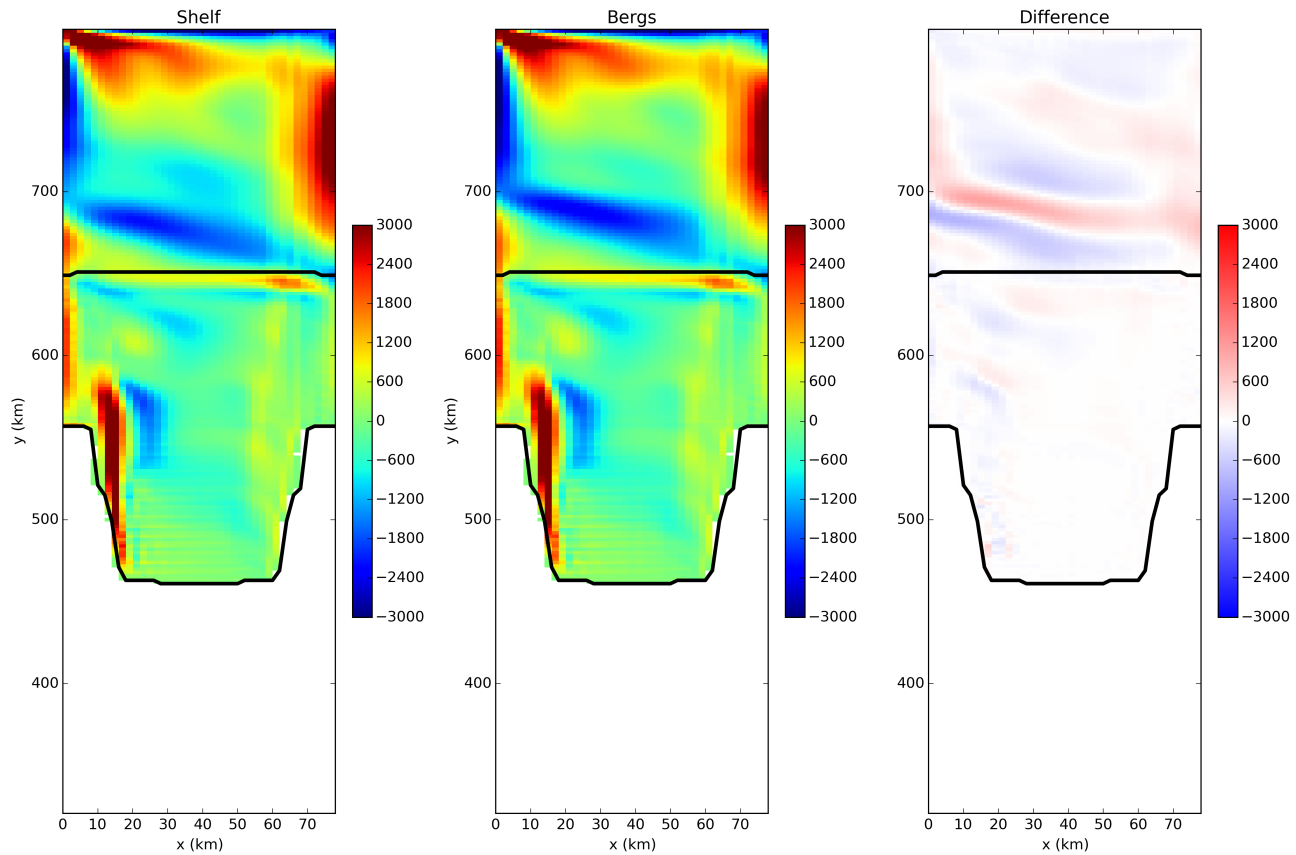


Figure S9. Layer: Comparison of Eulerian ice-shelf model and Lagrangian ice-shelf model barotropic stream function

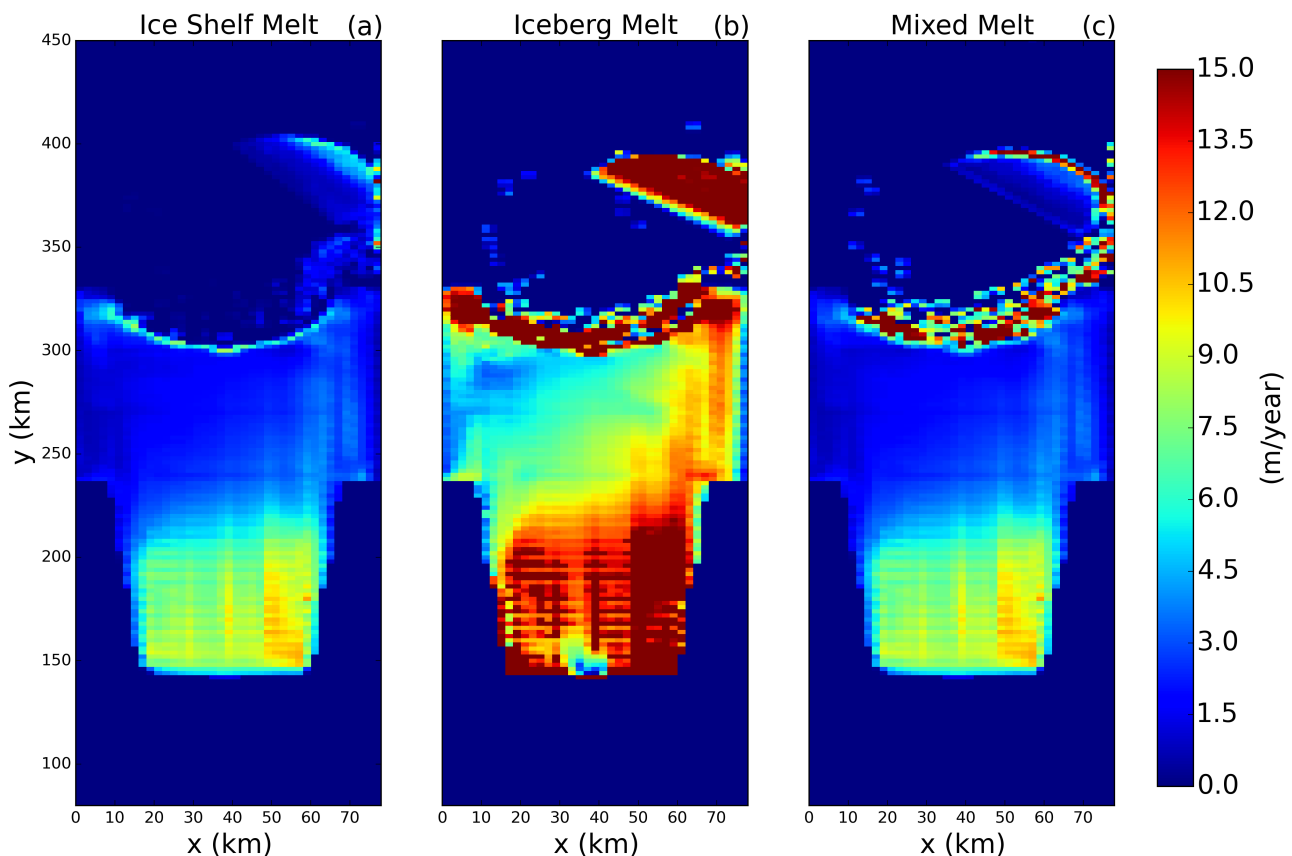


Figure S10. Comparison on melt rates using (a) three equation model, (b) iceberg melt parametrization, and (c) mixed melting.